
**1 Local wind regime induced by the presence of giant
2 linear dunes.**

**3 Cyril Gadal · Pauline Delorme ·
4 Clément Narteau · Giles F.S. Wiggs ·
5 Matthew Baddock · Joanna M. Nield ·
6 Philippe Claudin**

7
8 Received: DD Month YEAR / Accepted: DD Month YEAR

9 Abstract

10 In large-scale studies of arid areas, sediment fluxes and resulting geomorpho-
11 logical quantities (sediment pathways, erosion rates, dune morphodynamics)
12 are often derived from wind data. However, the feedback of nearby topogra-
13 phy on the flow, such as kilometric giant dunes, is rarely taken into account
14 because barely studied. Here, we compare locally measured wind data to the
15 predictions of the Era5Land climate reanalysis in four different places across
16 and around the Namib sand sea. In places with flat environments, we show
17 that the two wind datasets agree with each other. In contrast, within the
18 sand sea, we show that they significantly differ due to the presence of giant
19 linear dunes. We quantify this discrepancy, and link it to dynamics of the
20 atmospheric boundary layer. Aside setting limits to the applicability of the
21 Era5land dataset, this study highlights the giant dunes feedback on the wind,
22 and discuss its implications for smaller scale bedforms. All codes used, from
23 the raw data to the figures of the paper, are publicly available with full doc-
24 documentation at <https://github.com/Cgadal/GiantDunes> (will be made public
25 upon acceptance of this manuscript for publication).

26 **Keywords** Boundary layer · Turbulent flow · Sand dunes · Fluide-structures
27 interactions

C. Gadal

Institut de Mécanique des Fluides de Toulouse (IMFT), Université de Toulouse, CNRS,
INPT, UPS, Toulouse, France
E-mail: cyril.gadal@imft.fr

S. Author
second address

T. Author
third address

28 1 Introduction

29 As a flow encounters an obstacle, different interactions can arise depending on
30 the different time and length scales involved. In the case of atmospheric flows,
31 this mainly depends on the part of the atmosphere, schematically composed
32 of a turbulent boundary layer topped by a stably stratified one, with which
33 the obstacle interacts (Stull 1988). At the largest scale, the feedback of moun-
34 tains on the stratified free atmosphere results in wave generation as well as
35 significant wind disturbances, such as downslope winds in the lee side (Dur-
36 ran 1990). Inside the boundary layer, the interaction between a turbulent flow
37 and hilly surfaces is for example key to the understanding ocean surface wind-
38 driven waves (Sullivan and McWilliams 2010), or eolian bedforms in desert
39 (Courrech du Pont 2015).

40 Looking at the flow close to the surface, two different components of the
41 topography feedback can be isolated. First, the flow accelerates on the upwind
42 slope, and slows down on the downwind one, with a maximum velocity slightly
43 upwind of the crest (Jackson and Hunt 1975; Sykes 1980; Hunt et al. 1988).
44 Several measurements are available, performed in subaqueous flumes (Zilker
45 et al. 1977; Zilker and Hanratty 1979; Frederick and Hanratty 1988) and in
46 eolian field conditions (Claudin et al. 2013; Lü et al. 2021). Second, deflection
47 occurs when the incident flow direction is not perpendicular to the ridge crest.
48 While predicted to be small (less than 10°) in the linear regime (Gadal et al.
49 2019), significant flow steering has been reported in the field on the downwind
50 side of larger aspect ratios obstacles, such as mountain ranges (Kim et al. 2000;
51 Lewis et al. 2008; Fernando et al. 2019) or sand dunes (Walker et al. 2009;
52 Walker and Shugar 2013; Hesp et al. 2015; Smith et al. 2017).

53 In the case of aeolian bedforms, the measurements mentioned above were
54 made on dunes a few meters high only. The resulting wind disturbances have
55 then been shown to significantly impact the sediment pathways of the whole
56 system (Hesp et al. 2015), but also to affect the collective behaviour of dune
57 populations through long-range interactions (Bacik et al. 2020). However, eo-
58 lian dunes coexist in sand seas at different scales, each representative of their
59 different evolution stages, from emergence at twenty meters wavelengths to gi-
60 ant size, corresponding to kilometric wavelengths and heights of several dozen
61 meters (McKee 1979). Quantifying these two effects for giant dunes is then
62 all the more important for several reasons. First, larger wind disturbances
63 are expected from larger obstacles. Second, the flow–structure coupling is
64 not straightforward due to vertical structure of the atmosphere with which
65 the giant dunes interact due to their sizes (Andreotti et al. 2009). Finally,
66 the morphodynamics of aeolian bedforms are strongly dependent on the wind
67 regime (Livingstone and Warren 1996). Thus, small-scale bedforms are sen-
68 sitive to wind disturbances induced by larger-scale bedforms. This has been
69 demonstrated for impact ripples on dunes (Howard 1977; Hood et al. 2021),
70 but has never been studied for medium-scale dunes near giant dunes.

71 In the literature, arid areas have been studied at the desert scale from
72 climate reanalyses based on global atmospheric models (Blumberg and Greeley

73 1996; Livingstone et al. 2010; Ashkenazy et al. 2012; Jolivet et al. 2021; Hu
74 et al. 2021), such as ERA-40, ERA-Interim or ERA-5 (Uppala et al. 2005;
75 Dee et al. 2011; Hersbach et al. 2020). However, the spatial resolution (tens of
76 kilometers) of these reanalyses implies average quantities that do not resolve
77 the smaller scales, ranging from the study of individual dunes to the border of
78 mountains (Livingstone et al. 2010). Lately, the release of ERA5-Land allow to
79 push back this limitation by providing up to 70 years of hourly wind predictions
80 at a 9 km spatial resolution (Muñoz-Sabater et al. 2021). However, due to its
81 recent nature, the applicability limitations of this dataset remain to be studied.

82 Here, we compare local wind speeds and directions measured in four dif-
83 ferent places across the Namib desert to the regional predictions of the ERA5-
84 Land climate reanalysis. When the measurement stations are surrounded by a
85 relatively flat environment, we show that local measurements and regional pre-
86 dictions agree with each other. On the contrary, in the sand sea, we show that
87 they differ due to the presence of giant dunes. Furthermore, we link the magni-
88 tude of these discrepancies to the circadian cycle of the atmospheric boundary
89 layer. Finally, we draw implications for smaller-scale eolian bedforms.

90 2 Wind regimes across the Namib Sand Sea

91 We focus on four places across and nearby the Namib desert, highlighting
92 different environments (see Fig. 1). The Adamax station is located near the
93 Adamax salt pan, in a highly vegetated area. The Huab station, on the coast
94 at the outlet of the Huab river, is in an arid environment exhibiting 60-m scale
95 barchan dunes. While the surroundings of these two stations are relatively flat,
96 this is not the case for the Deep Sea and South Namib stations. Both are in
97 the interdune between tens of meters high giant linear dunes with kilomet-
98 ric wavelengths and superimposed patterns. In this section, we describe and
99 compare winds from local measurements and climate reanalysis predictions.

100 2.1 Datasets

101 Local winds are provided by measurement stations located in the four different
102 places (see black dots in Fig. 1). The wind strength and direction are sampled
103 every 10 minutes by cup anemometers and wind vanes, at heights between
104 2 m and 3 m depending on the station. The available period of measurements
105 ranges from 1 to 5 discontinuous years distributed between 2012 and 2020 (see
106 Fig. S1). We checked that at least one complete seasonal cycle is available at
107 each station. Regional winds are extracted at the same locations and periods
108 from the ERA5-Land dataset, which is a replay at a smaller spatial resolution
109 of ERA5, the latest climate reanalysis from the ECMWF (Hersbach et al.
110 2020; Muñoz-Sabater et al. 2021). It provides hourly predictions of the 10-m
111 wind velocity and direction at a spatial resolution of ~ 9 km ($0.1^\circ \times 0.1^\circ$).

112 For comparison, the local measurements are averaged into 1-hr bins cen-
113 tered on the temporal scale of the ERA5-Land estimates (see Fig. S2). As the

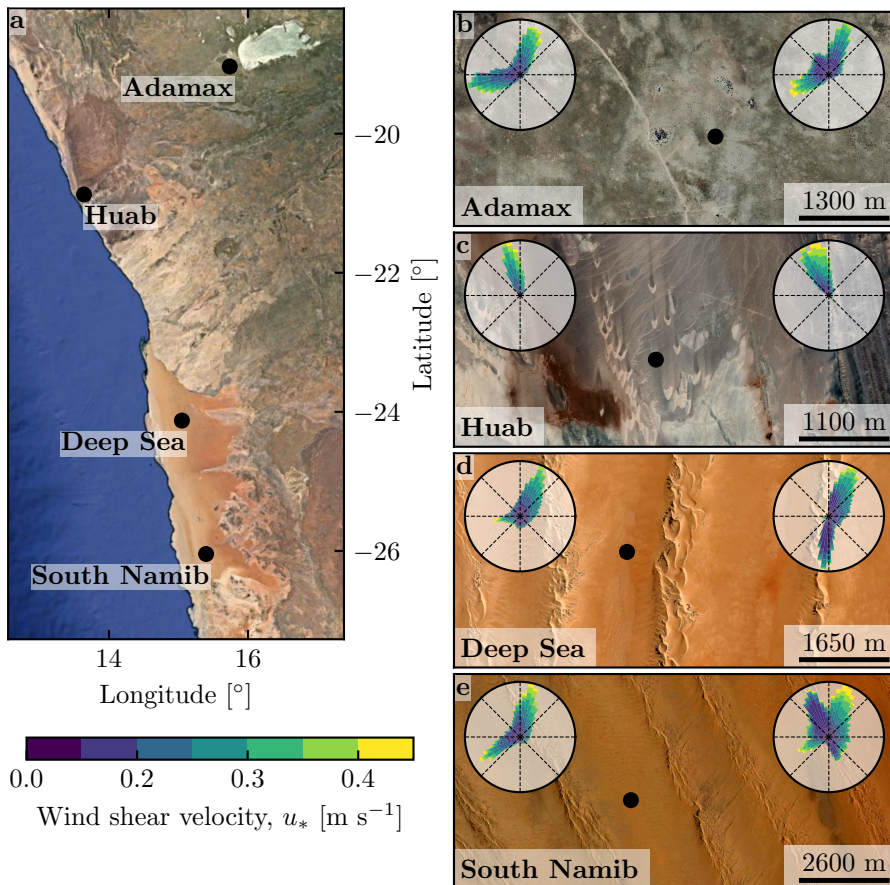


Fig. 1 Wind data used in this study **a**: Location of the studied sites. **b–e**: Satellite images of the studied sites (Google-Earth, Maxar Technologies, CNES/Airbus). In each subplot, the left and right wind roses represent the data from the ERA5Land climate reanalysis and the local wind stations, respectively. Note that the bars show the direction towards which the wind blows. The black dots show the location of local wind stations.

114 wind velocities of both datasets are provided at different heights, we convert
 115 them into shear velocities (see SI section 1), characteristic of the turbulent
 116 wind profile, which are then used together with the wind direction for further
 117 analysis. The resulting wind data are shown on the wind roses of Fig. 1(b–e).

118 Finally, the dune properties are computed using autocorrelation on the 30-
 119 m Digital Elevation Models (DEMs) of the shuttle radar topography mission
 120 (Farr et al. 2007). For the South Namib and Deep Sea stations, we obtain
 121 respectively orientations of 85° and 125° , wavelengths of 2.6 km and 2.3 km
 122 and amplitudes of 45 m and 20 m (see Fig. S4 for more details).

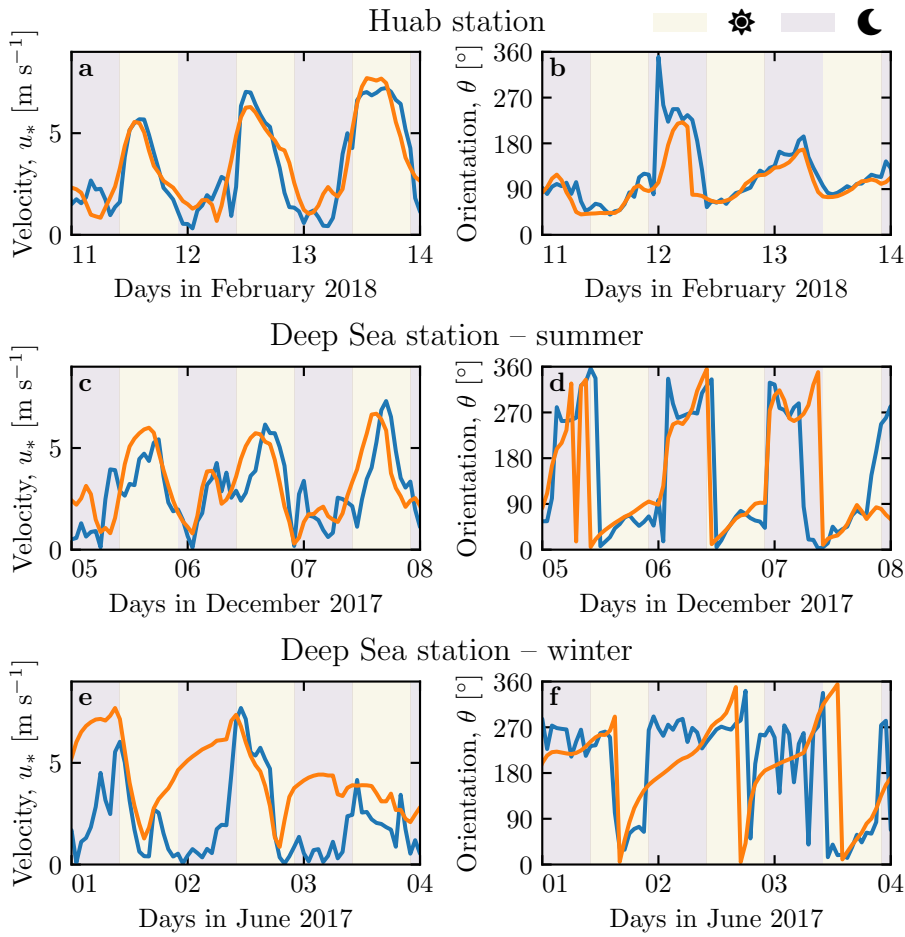


Fig. 2 Temporal comparison between the wind data coming from the Era5Land climate reanalysis (orange lines) and from the local measurements (blue lines). Color swathes indicate day (between 1000 UTC and 2200 UTC) and night (before 1000 UTC or after 2200 UTC) **a–b:** Huab station. **c–d:** Deep Sea station in winter. **e–f:** Deep Sea station in summer.

123 2.2 Agreement between local and regional winds

124 The obtained wind regimes are shown in figure 1. In the Namib, the regional
 125 wind patterns are essentially controlled by the see breeze, resulting in strong
 126 northward components (sometimes slightly deviated by the large scale topog-
 127 raphy) present in all regional wind roses (Lancaster 1985). These daytime
 128 winds are dominant during the second-half of the year (Septembre–January).
 129 In winter, an additional easterly component can be recorded during the night,
 130 induced by the combination of katabatic winds forming on the mountains,
 131 and infrequent ‘berg’ winds, which are responsible of the high wind velocities
 132 observed (Lancaster 1984). The frequency of these easterly components de-

creases from the inland to the coast, resulting in bidirectional wind regimes within the Namib Sand Sea and at the Adamax salt pan (Fig. 1b, 1d and 1e) and a unidirectional wind regime on the coast at the outlet of the Huab River (Fig. 1c).

In the case of the Adamax and Huab stations, the wind roses from the regional predictions qualitatively match those corresponding to the local measurements. However, for the Deep Sea and South Namib stations, the measured wind roses exhibit additional components aligned with the giant dune orientation visible on the satellite images (Fig. 1c–d). The time series of wind speed and direction show that this agreement in the case of Adamax and Huab stations is always verified (Fig. 2a–b) and Fig. S5). In contrast, for the stations within the giant dune field, we observe that this agreement is limited to Septembre–January time periods (Fig. 2c–d).

2.3 Influence of the giant dunes on local wind regimes

In the February–August period, when giant dunes are present, the local and regional winds match during daytime only, i.e when the southerly/southwesterly sea breeze dominates (see Fig. 2(e–f), Fig. 3 and Fig. S6). In the late afternoon and during the night, when the northwesterly ‘berg’ and katabatic winds blow, measurements and predictions differ. In this case, the angular wind distribution of the local measurements exhibits two additional modes separated of $\simeq 180^\circ$, each corresponding to the giant dune alignment (see the purple frame in Fig. 3 and Fig. S6, as well as Fig. S7). This deviation is also associated with a global attenuation of the wind strength (Fig. S8). Remarkably, all these figures show that this process occurs for low wind velocities, typically for $u_* < 0.1 \text{ m s}^{-1}$. For shear velocities larger than 0.25 m s^{-1} , this wind reorientation does not occur. Finally, for intermediate shear velocities, both reorientation along the dune crest and no reorientation are observed (Fig. S7).

3 Influence of the circadian cycle of the atmospheric boundary layer

For linear ridges, dune-induced flow disturbances have mainly been related to the angle between wind direction and crest orientation, with a maximum for angles between 30° and 70° (Walker et al. 2009; Hesp et al. 2015). In our case, the most deflected wind for both stations is the most perpendicular, such that the incident wind direction does not seem to be the dominant parameter controlling the wind deflection. In contrast, a different behavior is observed between low and high wind velocities, suggesting a change in hydrodynamical regime.

In the following, we discuss the relevant parameters leading to different hydrodynamical interactions with topographical obstacles, and interpret the data with respect to the corresponding physical mechanisms.

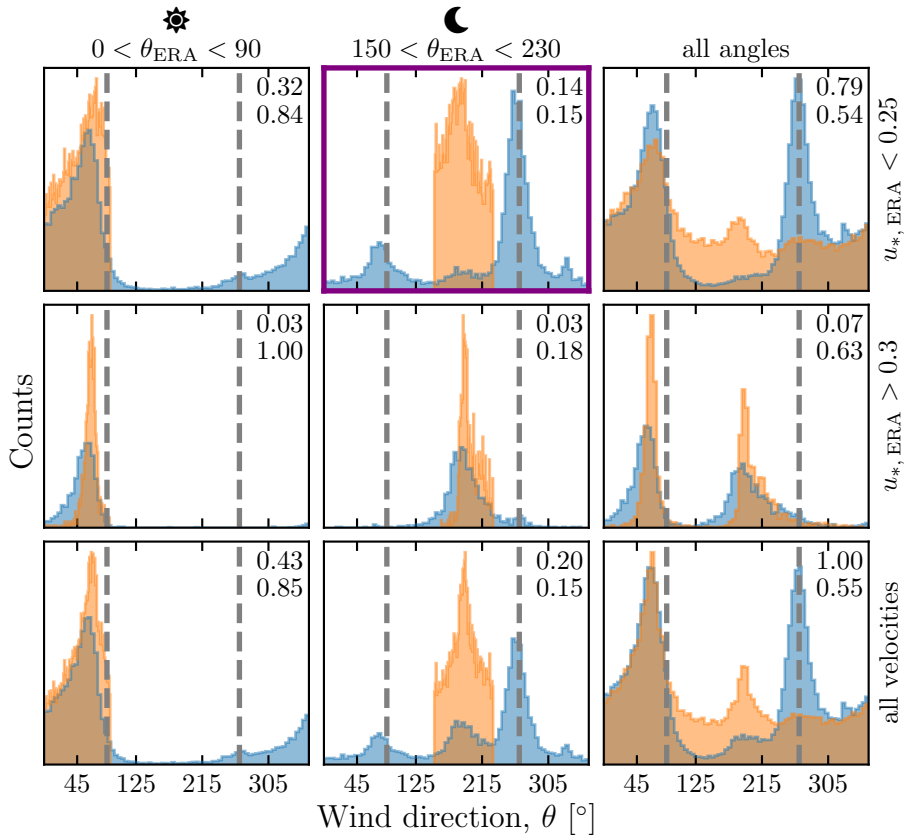


Fig. 3 Distributions of wind direction at the Deep Sea Station for the Era5Land climate reanalysis (orange) and the local measurements (blue). In each subplot, both distributions are plotted from the same time steps, selected with constraints on the wind direction (columns) and/or wind velocity (rows) of the Era5Land dataset. The gray vertical dashed lines indicate the dune orientation. The numbers at the top right give the percentage of time steps selected in each sub-range, as well as the percentage of them corresponding to the day (between 1000 UTC and 2200 UTC). The purple frame highlights the regime (small wind velocities, nocturnal summer wind) in which the data from both datasets differs. A similar figure can be obtained for the Deep Sea station (see Fig. S6).

173 3.1 Relevant non-dimensional parameters and physical considerations

174 Flow deflection over ridges can be understood from the Bernoulli principle (Hesp
 175 et al. 2015). As the flow approaches the ridge crest, the compression of the
 176 streamlines results in larger flow velocities, and thus lower pressures (Rubin
 177 and Hunter 1987). An incident flow oblique to the ridge is then deflected to-
 178 wards lower pressure zones, i.e towards the crest. Turbulent dissipation at the
 179 bottom and non-linearities tends to increase this effect downstream, resulting
 180 in along the crest wind deflection in the lee side (Hesp et al. 2015; Gadal et al.
 181 2019).

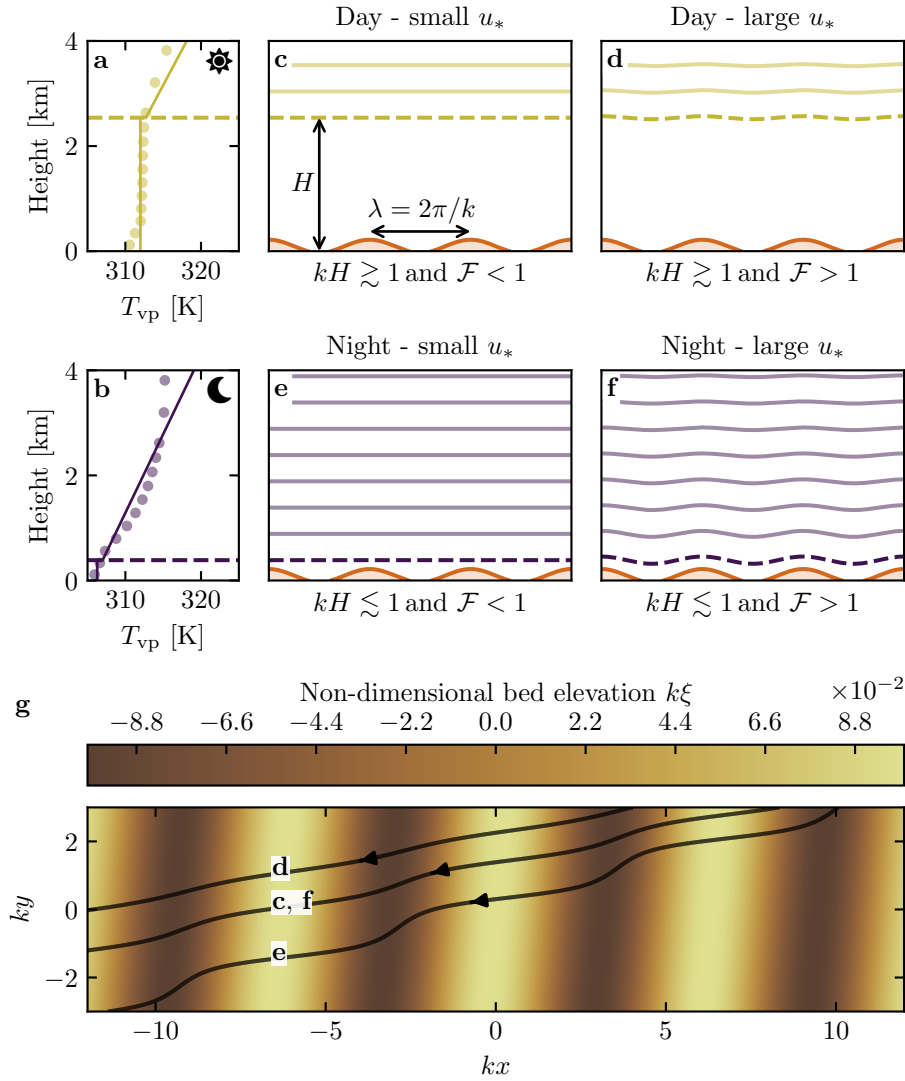


Fig. 4 **a–b:** Vertical profiles of the virtual potential temperature at 2 different time steps (day - 31/03/2017 - 1200 UTC, night - 21/03/2017 - 2200 UTC) at the Deep Sea station. Dots: data from the ERA5 reanalysis. Transparent dashed lines: boundary layer height given by the ERA5 reanalysis, calculated from the bulk Richardson number (Seidel et al. 2012). Plain lines: vertical (boundary layer) and linear (free atmosphere) fits to estimate the stratification properties. **c–f:** Sketches representing the interaction between the giant dunes and the atmospheric flow for different meteorological conditions. **g:** Streamlines qualitatively representing the effect of low, medium and high flow confinement. For details on the streamline derivation, see Appendix 4.

Another way to increase the flow deflection is its confinement below a capping surface, that results in further streamline compression. This is the case for bedforms forming in open channel flows such as rivers (Fourrière et al. 2010; Unsworth et al. 2018), but also for eolian dunes. These dunes evolve in the turbulent atmospheric boundary layer (ABL), which is capped by a transitional layer separating it from the stratified atmosphere above (see Fig. 4). Two different mechanisms control the possibility of this additional streamline compression.

On one hand, it depends if the flow disturbance induced by the underlying topography reach the surface. As obstacles typically disturb flow over a characteristic height similar to their length, the potential of interaction between the dunes and the overlying surface is well captured by the parameter kH , where $k = 2\pi/\lambda$ is the wavenumber and H the ABL depth. Note that H is directly related to the radiative fluxes at the Earth surface, and thus varies with the circadian and seasonal cycles. Here, the giant dunes have kilometric wavelengths, such that $0.02 \lesssim kH \lesssim 5$, and they interact most of the time with the capping layer and the stratified free atmosphere (FA) above (Andreotti et al. 2009). Interestingly, the limit of no-interactions between the topography and the boundary layer structure ($kH \gg 1$), in which the properties of the overlying atmospheric structure are irrelevant, is never reached here, in the case of giant dunes.

On the other hand, it depends on rigidity of the capping surface, as its deformation releases the confinement effect inducing streamline compression. This is typically quantified using the Froude number (Vosper 2004; Stull 2006; Sheridan and Vosper 2006; Hunt et al. 2006; Jiang 2014):

$$\mathcal{F} = \frac{U}{\sqrt{\frac{\Delta\rho}{\rho_0} g H}}, \quad (1)$$

where U is the wind velocity at the top of the ABL, ρ_0 its average density, $\Delta\rho$ the density jump between the ABL and the FA.

The smallest wind disturbances are expected during the day, when the ABL depth is comparable to the dune wavelength ($kH \gtrsim 1$) and for large wind velocities, which correspond to a weak confinement situation (Fig. 4d). On the contrary, large wind disturbances are expected to occur during the night, when the confinement is mainly induced by shallow ABL (Fig. 4e–f). Note that this strong confinement can be somewhat reduced in the case of strong winds (corresponding to large Froude numbers, see Fig. 4f), explaining the transition from deflected to non-deflected winds related to low and high velocities observed in the data (see section 2.3).

3.2 Flow regime diagrams

To highlight these different regimes from our data, we compute wind disturbance diagrams in the space defined by the two relevant non-dimensional

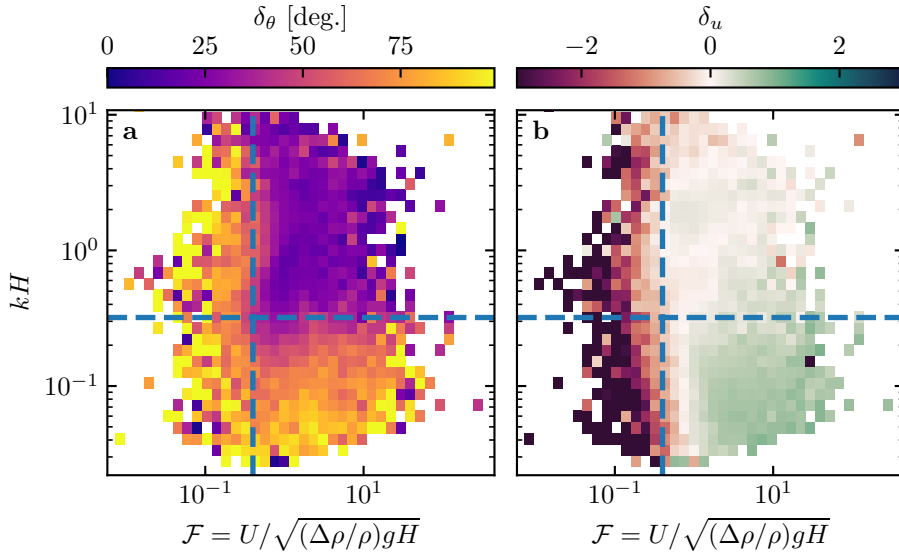


Fig. 5 Regime diagrams of the wind deviation δ_θ and relative attenuation/amplification δ_u in the space (\mathcal{F}, kH) , containing the data from both the Deep Sea and South Namib stations. Blue dashed lines empirically delimit the different regimes. The point density in each bin of the diagrams is shown in Fig. S11. The regime diagrams in the spaces (\mathcal{F}_1, kH) and $(\mathcal{F}_1, \mathcal{F})$ are shown in Fig. S12.

numbers presented above, (kH, \mathcal{F}) . Those are calculated from the time series of the geopotential, temperature and specific humidity vertical profiles available in the ERA5 climate reanalysis (see SI section 2). Flow deviation is computed as the minimal angle between the wind orientations from the local measurements, and the regional predictions. The relative velocity modulation is computed as

$$\delta_u = \frac{u_*^{\text{ERA}} - u_*^{\text{station}}}{u_*^{\text{ERA}}}. \quad (2)$$

When representing the two variables δ_θ and δ_u in this space, different regime emerges (Fig. 5). Small wind disturbances ($\delta_\theta \rightarrow 0, \delta_u \rightarrow 0$) are located in the top-right part of the diagrams, corresponding to a regime mixing low-interaction and low-confinement (kH and \mathcal{F} large enough, Fig. 4d). Lower values of kH (stronger interaction) or Froude number (stronger confinement) then both lead to an increase in wind disturbances, both in terms of orientation and velocity. Below a threshold value of $kH \simeq 0.3$, wind disturbance occurs independently of the Froude number value, probably due to enhanced non-linear effects linked to strong flow modulation by the obstacle in this part of the diagram. The Froude number also controls a transition from damped to amplified wind velocities in the interdune, with a transition at $\mathcal{F} \simeq 0.4$ (Fig. 5b). This may be linked to a transition in the flow regime in the lee side of the obstacle (lee waves, hydraulic jumps, rotors) but further measurements are needed in order to assess this (Baines 1995; Vosper 2004).

241 3.3 On the influence of the stratification of the free atmosphere

242 The presence of a stratification in the free atmosphere can also impact the
 243 flow confinement, depending on its ability to deform under the presence of an
 244 underlying obstacle. This can be quantified using the internal Froude num-
 245 ber (Vosper 2004; Stull 2006; Sheridan and Vosper 2006; Hunt et al. 2006;
 246 Jiang 2014):

$$\mathcal{F}_I = \frac{kU}{N}, \quad (3)$$

247 where $N = \sqrt{-(g/\rho_0)(\partial\rho/\partial z)}$ is characteristic of the stratification. Both
 248 Froude numbers have the same qualitative effect on flow confinement, as they
 249 quantify the rigidity of the overlying layers. This is confirmed by figure S12,
 250 where we can also find the different regimes related to wind disturbances de-
 251 scribed previously for the Froude number \mathcal{F} .

252 **4 Discussion**

253 The comparison of local (direct measurements) and regional (climate reanal-
 254 ysis) wind data reveals the giant dunes feedback on the flow. In flat areas,
 255 the matching between measurements and prediction confirms the ability of the
 256 ERA5Land climate reanalysis to predict the wind flow down to scales ~ 10 km,
 257 i.e the grid model. When smaller scale topographies are present (giant dunes
 258 in our case), locally measured wind regimes can significantly differ from the
 259 regionally predicted ones. Furthermore, we link these disturbances induced by
 260 the dunes to their interaction with the lower part of the atmospheric vertical
 261 structure, and more specifically to its circadian variability. During the night,
 262 the presence of a shallow atmospheric boundary layer (ABL) induces a strong
 263 confinement of the flow, associated with large wind deviation and acceleration
 264 or deceleration. During the day, the capping layer is high enough to prevent
 265 its interaction with the giant dunes, resulting in a low confinement of the flow,
 266 and thus smaller wind disturbances. Interestingly, we also found that this ef-
 267 fect could be counterbalanced by the presence of large wind velocities, capable
 268 of deforming the capping layer and/or the FA stratification, thus decreasing
 269 the confinement effect.

270 Simple linear models also suggest that larger wind disturbances occur un-
 271 der strong flow confinement such as described above Andreotti et al. (2009,
 272 2012). However, they are unable to reproduce the magnitude of the observed
 273 deviations, probably due to the presence of hydrodynamical non-linear effects,
 274 all the more present in high confinement situations linked to strong flow mod-
 275 ulations (see Fig. S12 and Appendix 1). They also predict different spatial flow
 276 structures such as lee waves and rotors (Baines 1995; Vosper 2004), which are
 277 likely to be complicated by these non-linearities, and which cannot be observed
 278 by our single point measurements. Measurements in different places along and
 279 across the ridge are then needed in order to properly map these flow structures,
 280 and allow further comparisons with models.

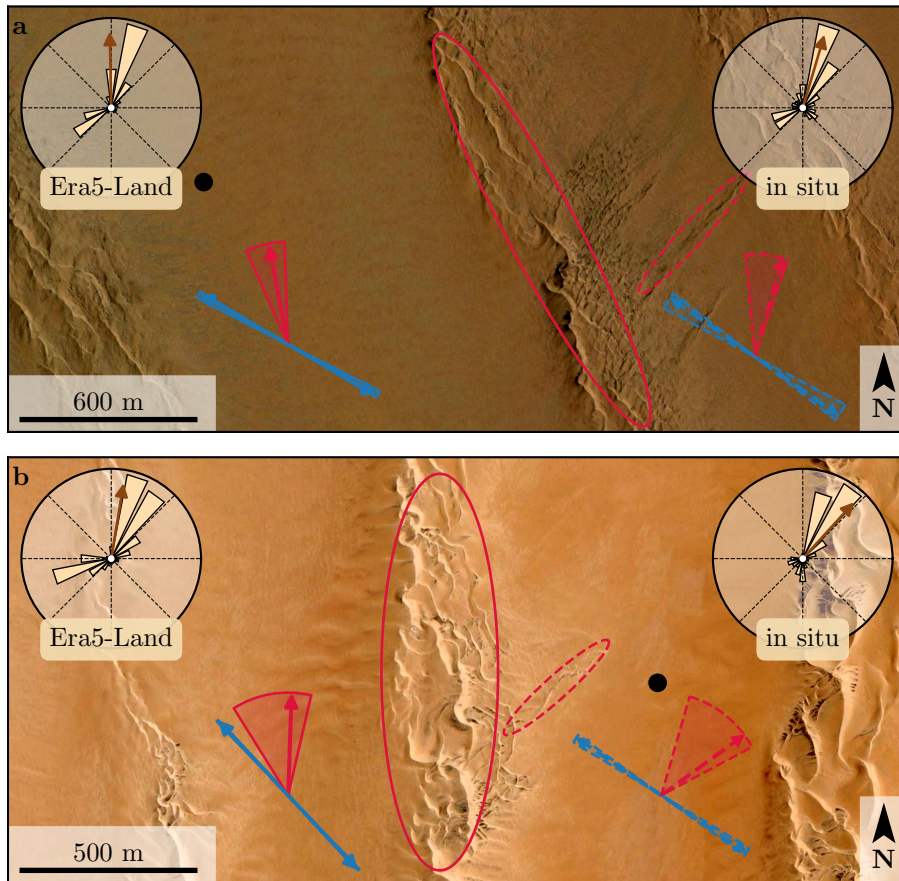


Fig. 6 Implications for smaller scale patterns in (a) the South Namib and (b) Deep Sea. The ellipses indicates the different types of elongating dunes, at large (plain) and small scale (dashed). The dune orientations are calculated using the model of Courrech du Pont et al. (2014) from the sand flux angular distributions, shown here for typical sand quartz grains of $180\ \mu\text{m}$. The double blue and single red arrows correspond to the two possible dune growth mechanisms, bed instability and elongation, respectively. Likewise, plain arrows are calculated from the ERA5-Land data, and dashed arrows from the local measurements. Wedges show the uncertainty on the orientation calculation, and the arrows correspond to typical parameters found in the literature, i.e. a grain diameter of $180\ \mu\text{m}$ and a flux-up ratio of 1.6. The black dots indicate the position of the measurement stations. See Appendix 2 for additional details.

This study highlights the interaction between giant dunes and the atmospheric boundary layer. It then supports the debated idea that the capping layer acts as a bounding surface limiting dune growth (Andreotti et al. 2009), as opposed to an unconstrained growth ever-slower with size (Eastwood et al. 2011; Gunn et al. 2021). Once validated, this mechanism would then allow inference of the ABL depth from the giant bedforms spacing where measure-

287 ments are not feasible or available, as performed by Lorenz et al. (2010) on
 288 Titan.

289 This interaction also have strong implications for smaller scales bedforms,
 290 as illustrated in Fig. 6. In the Namib Sand Sea, small linear dunes (~ 50 m
 291 -wide) are present in the interdune between giant linear dunes (~ 2 km -wide).
 292 While differences between larger and smaller scale dune patterns are observed
 293 ubiquitously, they are now largely attributed to the presence of two different
 294 dune growth mechanisms, leading to two different dune patterns (orientations
 295 and/or morphologies) for the same wind regime (Courrech du Pont et al.
 296 2014; Runyon et al. 2017; Lü et al. 2017; Song et al. 2019; Hu et al. 2021).
 297 Here, coupling sediment transport and dune growth models, we show that the
 298 orientations of the small and giant linear dunes can be predicted from the same
 299 dune growth mechanism, using the locally measured and regionally predicted
 300 winds, respectively (red arrows in Fig. 6). The giant dune feedback on the
 301 flow described in this study then provides a mechanism for the existence of
 302 these small linear dunes elongating across the interdune, as yet unresolved.
 303 While further studies are needed, these dune type could provide additional
 304 strong constraints for the inference of local winds from bedforms, as currently
 305 performed on Mars using ripple orientations (Liu and Zimbelman 2015; Hood
 306 et al. 2021).

307 **Acknowledgements** We would like to acknowledge the contributors of the following open-
 308 source python librairies, Matplotlib (Hunter 2007), Numpy (Harris et al. 2020) and Scipy
 309 (Virtanen et al. 2020), which provide an incredibly efficient ecosystem allowing scientific
 310 research in Python.

311 Era5 and Era5Land datasets are publicly available at the Copernicus Climate Change
 312 Service (C3S) Climate Data Store. The locally measured wind data can be found at [up-](#)
 313 [load on public data repository](#). The digital elevation models from the Shuttle Radar To-
 314 polography Mission are publicly available from Nasa servers, and can be downloaded at
 315 <https://dwtkns.com/srtm30m/>. Fully documented codes used to analyze this study are
 316 available at <https://github.com/Cgadal/GiantDunes> (will be made public upon acceptance
 317 of this manuscript for publication).

318 [citing all grants ...]

319

320 Appendix 1: ABL turbulent wind model

321 Following the work of Fourrière et al. (2010), Andreotti et al. (2012) and Andreotti
 322 et al. (2009), we briefly expose in this section the linear response of a
 323 turbulent flow to a small aspect ratio perturbation of the underlying topogra-
 324 phy. As this topography can be decomposed into several sinusoidal modes, we
 325 focus on a sinusoidal topography:

$$\xi = \xi_0 \cos [k (\cos(\alpha)x + \sin(\alpha)y)], \quad (4)$$

326 which is also a good approximation for the giant dunes observed in the Deep
 327 Sea and South Namib Station (see Fig 1 and Fig S4). Here, x and y are
 328 the streamwise and spanwise coordinates, $k = 2\pi/\lambda$ the wavenumber of the

329 sinusoidal perturbation, and α its crest orientation, calculated with respect to
 330 the y -direction.

331 The two components of the basal shear stress $\tau = \rho_0 u_* \mathbf{u}_*$, constant in a
 332 flat bottom situation, can then be written without loss of generality as:

$$\tau_x = \tau_0 \left(1 + k\xi_0 \sqrt{\mathcal{A}_x^2 + \mathcal{B}_x^2} \cos [k(\cos(\alpha)x + \sin(\alpha)y) + \phi_x] \right), \quad (5)$$

$$\tau_y = \tau_0 k\xi_0 \sqrt{\mathcal{A}_y^2 + \mathcal{B}_y^2} \cos [k(\cos(\alpha)x + \sin(\alpha)y) + \phi_y], \quad (6)$$

333 where τ_0 is the basal shear stress on a flat bed, and $\phi_{x,y} = \tan^{-1}(\mathcal{B}_{x,y}/\mathcal{A}_{x,y})$.
 334 The in-phase and in-quadrature hydrodynamical coefficients $\mathcal{A}_{x,y}$ and $\mathcal{B}_{x,y}$
 335 are functions of the flow conditions, i.e the bottom roughness, the vertical
 336 flow structure or the incident flow direction (Fourrière et al. 2010; Andreotti
 337 et al. 2009, 2012).

338 Following Andreotti et al. (2012), the impact of the incident wind direction
 339 can be approximated by the following expressions:

$$\mathcal{A}_x = \mathcal{A}_0 \cos^2 \alpha, \quad (7)$$

$$\mathcal{B}_x = \mathcal{B}_0 \cos^2 \alpha, \quad (8)$$

$$\mathcal{A}_y = \frac{1}{2} \mathcal{A}_0 \cos \alpha \sin \alpha, \quad (9)$$

$$\mathcal{B}_y = \frac{1}{2} \mathcal{B}_0 \cos \alpha \sin \alpha, \quad (10)$$

340 where \mathcal{A}_0 and \mathcal{B}_0 are now two coefficients independent of the dune orientation
 341 α . In the case of a fully turbulent boundary layer capped by a stratified atmo-
 342 sphere, they now only depend on kH , kz_0 , \mathcal{F} and \mathcal{F}_I Andreotti et al. (2009).
 343 In this study, we assume a constant hydrodynamic roughness $z_0 \sim 1$ mm,
 344 leading to a constant value of $kz_0 \sim 10^{-6}$. Measured values of z_0 in the field
 345 indeed reports a variation of z_0 between 0.1 mm and 10 mm (Sherman and
 346 Farrell 2008; Field and Pelletier 2018), but \mathcal{A}_0 and \mathcal{B}_0 does not vary much in
 347 the corresponding range of kz_0 (Fourrière et al. 2010). Note that the linearity
 348 assumption of this theoretical framework requires $(|\tau| - \tau_0)/\tau_0 \ll 1$, which is
 349 satisfied by $k\xi \sqrt{\mathcal{A}_0^2 + \mathcal{B}_0^2} \ll 1$. In our case, the giant dune morphology gives
 350 $k\xi \simeq 0.1$, setting the upper bound of the coefficient modulus $\sqrt{\mathcal{A}_0^2 + \mathcal{B}_0^2}$ to 10.

351 Additionally, we also calculate the time series of the hydrodynamical coeffi-
 352 cients from the time series of the non-dimensional numbers used in this study.
 353 The results, shown Fig. S12 under the similar form of the regime diagrams
 354 presented in Fig. 5 and Fig. S12, exhibit a qualitative matching with the ob-
 355 servations presented in this study. Small values of these coefficients ($\mathcal{A}_0 \simeq 3.4$
 356 and $\mathcal{B}_0 \simeq 1$) are found in low confinement cases, i.e for $kH \gg 1$ (no inter-
 357 action between the dunes and the capping layer) or for $kH \gg 1$ but large
 358 enough Froude numbers (reduced flow confinement due to the deformation of
 359 the overlying capping layer and stratification). In contrast, larger values are
 360 obtained in high confinement cases (small kH and Froude numbers). How-
 361 ever, not that most of this part of the diagrams are outside of the linear limit

362 discussed above ($\sqrt{A_0^2 + B_0^2} \gtrsim 10$), which does not allow further quantitative
 363 comparison with the data.

364 Appendix 2: Sediment transport and dune morphodynamics

365 Here, we briefly describe the sediment transport and dune morphodynamics
 366 theoretical framework leading to the prediction of sand fluxes and dune orient-
 367 tations from wind data.

368 *Sediment transport* The prediction of sand fluxes from wind data has been
 369 a long standing issue in geomorphological studies (Fryberger and Dean 1979;
 370 Pearce and Walker 2005; Sherman and Li 2012; Shen et al. 2019). Based on lab-
 371 oratory studies in wind tunnels (Rasmussen et al. 1996; Iversen and Rasmussen
 372 1999; Creyssels et al. 2009; Ho et al. 2011), as well as physical considerations
 373 (Ungar and Haff 1987; Andreotti 2004; Durán et al. 2011; Páhtz and Durán
 374 2020), it has been shown that the steady saturated sand flux over a flat sand
 375 bed depends linearly on the shear stress:

$$\frac{q_{\text{sat}, t}}{Q} = \Omega \sqrt{\Theta_{\text{th}}} (\Theta_t - \Theta_{\text{th}}), \quad (11)$$

376 where Ω is a proportionality constant, $Q = d\sqrt{(\rho_s - \rho_0)gd/\rho_0}$ is a character-
 377 istic flux, $\Theta = \rho_0 u_{*,t}^2 / (\rho_s - \rho_0)gd$ the Shields number, and Θ_{th} its threshold
 378 value for incipient sediment transport. Here, $\rho_s = 2.6 \text{ g cm}^{-3}$ and $d = 180 \mu\text{m}$
 379 are the grain density and diameter, and g is the gravitational acceleration.

380 Recently, Páhtz and Durán (2020) suggested a quadratic dependency on
 381 the shear stress by taking into account grain–grain interactions within the
 382 transport layer, performing better at reproducing laboratory data at high wind
 383 velocities:

$$\frac{q_{\text{sat}, t}}{Q} = \frac{2\sqrt{\Theta_{\text{th}}}}{\kappa\mu} (\Theta_t - \Theta_{\text{th}}) \left(1 + \frac{C_M}{\mu} [\Theta_t - \Theta_{\text{th}}] \right), \quad (12)$$

384 where $\kappa = 0.4$ is the von Kármán constant, $C_M = 1.7$ a constant and μ a
 385 friction coefficient, taken to be the avalanche slope of the granular material,
 386 i.e. ~ 0.6 . The fit of this law to the experimental data of Creyssels et al. (2009)
 387 and Ho et al. (2011) gives $\Theta_{\text{th}} = 0.0035$. The sand flux angular distributions
 388 and the dune orientations in Fig. 6 are calculated using this quartic law (12).
 389 However, we verified that using the quadratic law (11) instead did not change
 390 the predicted dune orientations by more than a few degrees.

391 *Dune orientations* The dune orientations are predicted from the computed
 392 sand flux time series, using the dimensional model of Courrech du Pont et al.
 393 (2014). Two orientations are possible depending on the mechanism dominating
 394 the dune growth: elongation or bed instability (the latter is also known as the
 395 rule of maximum gross bedform-normal transport from Rubin and Hunter
 396 (1987)).

³⁹⁷ The orientation α corresponding the bed instability is then the one that
³⁹⁸ maximizes the following growth rate:

$$\sigma \propto \frac{1}{H_d W_d T} \int_t q_{\text{crest},t} |\sin(\theta_t - \alpha)|, \quad (13)$$

³⁹⁹ where H_d and W_d are dimensional constants representing the dune height and
⁴⁰⁰ width, respectively. The flux at the crest is expressed as:

$$q_{\text{crest},t} = q_{\text{sat},t} [1 + \gamma |\sin(\theta_t - \alpha)|], \quad (14)$$

⁴⁰¹ where the flux-up ratio γ has been calibrated to 1.6 using field studies, under-
⁴⁰² water laboratory experiments and numerical simulations. Similarly, the dune
⁴⁰³ orientation corresponding to the elongation mechanism is the one that verifies:

$$\tan(\alpha) = \frac{\langle q_{\text{crest},t}(\alpha) \mathbf{e}_{\theta_t} \rangle \cdot \mathbf{e}_{WE}}{\langle q_{\text{crest},t}(\alpha) \mathbf{e}_{\theta_t} \rangle \cdot \mathbf{e}_{SN}}, \quad (15)$$

⁴⁰⁴ where $\langle \cdot \rangle$ denotes a vectorial time average. The unitary vectors \mathbf{e}_{WE} , \mathbf{e}_{SN} and
⁴⁰⁵ \mathbf{e}_{θ_t} are in the West–East, South–North and wind direction, respectively.

⁴⁰⁶ The resulting computed dune orientations, blue and red arrows in figure 6,
⁴⁰⁷ are then depending on a certain number of parameters (grain properties, flux-
⁴⁰⁸ up ratio), for which we took typical values for eolian desert on Earth. Due to
⁴⁰⁹ the lack of measurements in the studied places, significant uncertainties can
⁴¹⁰ however be expected. We therefore run a sensibility test by calculating the
⁴¹¹ dune orientations for grain diameters ranging from 100 μm to 400 μm and the
⁴¹² speed-up ratio from 0.1 to 10 (wedges on figure 6).

413 **References**

- 414 Andreotti B (2004) A two-species model of aeolian sand transport. *J Fluid
415 Mech* 510(510):47–70, DOI 10.1017/S0022112004009073
- 416 Andreotti B, Fourrière A, Ould-Kaddour F, Murray B, Claudin P (2009) Gi-
417 ant aeolian dune size determined by the average depth of the atmospheric
418 boundary layer. *Nature* 457(7233):1120–1123
- 419 Andreotti B, Claudin P, Devauchelle O, Durán O, Fourrière A (2012) Bedforms
420 in a turbulent stream: ripples, chevrons and antidunes. *Journal of Fluid
421 Mechanics* 690:94–128
- 422 Ashkenazy Y, Yizhaq H, Tsoar H (2012) Sand dune mobility under climate
423 change in the kalahari and australian deserts. *Climatic Change* 112(3):901–
424 923
- 425 Bacik KA, Lovett S, Colm-cille PC, Vriend NM (2020) Wake induced long
426 range repulsion of aqueous dunes. *Physical review letters* 124(5):054,501
- 427 Baines PG (1995) Topographic effects in stratified flows. Cambridge university
428 press
- 429 Blumberg DG, Greeley R (1996) A comparison of general circulation model
430 predictions to sand drift and dune orientations. *Journal of Climate*
431 9(12):3248–3259
- 432 Claudin P, Wiggs GFS, Andreotti B (2013) Field evidence for the upwind
433 velocity shift at the crest of low dunes. *Boundary-layer Meteorol* 148(1):195–
434 206, DOI 10.1007/s10546-013-9804-3
- 435 Courrech du Pont S (2015) Dune morphodynamics. *Comptes Rendus Physique*
436 16(1):118–138
- 437 Courrech du Pont S, Narteau C, Gao X (2014) Two modes for dune orientation.
438 *Geology* 42(9):743–746
- 439 Creyssels M, Dupont P, El Mohtar AO, Valance A, Cantat I, Jenkins JT, Pasini
440 JM, Rasmussen KR (2009) Saltating particles in a turbulent boundary layer:
441 experiment and theory. *Journal of Fluid Mechanics* 625:47–74
- 442 Dee DP, Uppala SM, Simmons AJ, Berrisford P, Poli P, Kobayashi S, Andrae
443 U, Balmaseda M, Balsamo G, Bauer dP, et al. (2011) The era-interim re-
444 analysis: Configuration and performance of the data assimilation system.
445 *Quarterly Journal of the royal meteorological society* 137(656):553–597
- 446 Durán O, Claudin P, Andreotti B (2011) On aeolian transport: Grain-scale
447 interactions, dynamical mechanisms and scaling laws. *Aeolian Research*
448 3(3):243–270, DOI 10.1016/j.aeolia.2011.07.006
- 449 Durran DR (1990) Mountain waves and downslope winds. In: *Atmospheric
450 processes over complex terrain*, Springer, pp 59–81
- 451 Eastwood E, Nield J, Baas A, Kocurek G (2011) Modelling controls on aeolian
452 dune-field pattern evolution. *Sedimentology* 58(6):1391–1406
- 453 Farr TG, Rosen PA, Caro E, Crippen R, Duren R, Hensley S, Kobrick M,
454 Paller M, Rodriguez E, Roth L, et al. (2007) The shuttle radar topography
455 mission. *Reviews of geophysics* 45(2)
- 456 Fernando H, Mann J, Palma J, Lundquist JK, Barthelmie RJ, Belo-Pereira M,
457 Brown W, Chow F, Gerz T, Hocut C, et al. (2019) The perdigao: Peering

- 458 into microscale details of mountain winds. *Bulletin of the American Meteorological Society* 100(5):799–819
459
- 460 Field JP, Pelletier JD (2018) Controls on the aerodynamic roughness length
461 and the grain-size dependence of aeolian sediment transport. *Earth Surface
462 Processes and Landforms* 43(12):2616–2626, DOI 10.1002/esp.4420
- 463 Fourrière A, Claudin P, Andreotti B (2010) Bedforms in a turbulent stream:
464 formation of ripples by primary linear instability and of dunes by nonlinear
465 pattern coarsening. *Journal of Fluid Mechanics* 649:287–328
- 466 Frederick KA, Hanratty TJ (1988) Velocity measurements for a turbulent non-
467 separated flow over solid waves. *Experiments in fluids* 6(7):477–486
- 468 Fryberger SG, Dean G (1979) Dune forms and wind regime. A study of global
469 sand seas 1052:137–169
- 470 Gadal C, Narteau C, Courrech Du Pont S, Rozier O, Claudin P (2019) Incip-
471 ient bedforms in a bidirectional wind regime. *Journal of Fluid Mechanics*
472 862:490–516
- 473 Gunn A, Wanker M, Lancaster N, Edmonds DA, Ewing RC, Jerolmack DJ
474 (2021) Circadian rhythm of dune-field activity. *Geophysical Research Letters*
475 48(5):e2020GL090,924
- 476 Harris CR, Millman KJ, van der Walt SJ, Gommers R, Virtanen P, Cournapeau D,
477 Wieser E, Taylor J, Berg S, Smith NJ, et al. (2020) Array program-
478 ming with numpy. *Nature* 585(7825):357–362
- 479 Hersbach H, Bell B, Berrisford P, Hirahara S, Horányi A, Muñoz-Sabater
480 J, Nicolas J, Peubey C, Radu R, Schepers D, et al. (2020) The era5
481 global reanalysis. *Quarterly Journal of the Royal Meteorological Society*
482 146(730):1999–2049
- 483 Hesp PA, Smyth TAG, Nielsen P, Walker IJ, Bauer BO, Davidson-Arnott R
484 (2015) Flow deflection over a foredune. *Geomorphology* 230:64–74
- 485 Ho TD, Valance A, Dupont P, Ould El Moctar A, Tuan Duc H, Valance A,
486 Dupont P, Ould El Moctar A (2011) Scaling laws in aeolian sand transport.
487 *Physical Review Letters* 106(9):4–7, DOI 10.1103/PhysRevLett.106.094501
- 488 Hood DR, Ewing RC, Roback KP, Runyon K, Avouac JP, McEnroe M (2021)
489 Inferring airflow across martian dunes from ripple patterns and dynamics.
490 *Frontiers in Earth Science* 9:Art-No
- 491 Howard AD (1977) Effect of slope on the threshold of motion and its applica-
492 tion to orientation of wind ripples. *Geological Society of America Bulletin*
493 88(6):853–856
- 494 Hu Z, Gao X, Lei J, Zhou N (2021) Geomorphology of aeolian dunes in the
495 western sahara desert. *Geomorphology* 392:107,916
- 496 Hunt J, Leibovich S, Richards K (1988) Turbulent shear flows over low hills.
497 *Quarterly Journal of the Royal Meteorological Society* 114(484):1435–1470
- 498 Hunt JCR, Vilenski GG, Johnson ER (2006) Stratified separated flow around
499 a mountain with an inversion layer below the mountain top. *Journal of Fluid
500 Mechanics* 556:105–119
- 501 Hunter JD (2007) Matplotlib: A 2d graphics environment. *Computing in sci-
502 ence & engineering* 9(03):90–95

- 503 Iversen JD, Rasmussen KR (1999) The effect of wind speed and bed slope on
504 sand transport. *Sedimentology* 46:723–731
- 505 Jackson PS, Hunt JCR (1975) Turbulent wind flow over a low hill. *Quarterly
506 Journal of the Royal Meteorological Society* 101(430):929–955
- 507 Jiang Q (2014) Applicability of reduced-gravity shallow-water theory to
508 atmospheric flow over topography. *Journal of the Atmospheric Sciences*
509 71(4):1460–1479
- 510 Jolivet M, Braucher R, Dovchintseren D, Hocquet S, Schmitt J, ASTER Team
511 (2021) Erosion around a large-scale topographic high in a semi-arid sedimen-
512 tary basin: Interactions between fluvial erosion, aeolian erosion and aeolian
513 transport. *Geomorphology* 386:107,747
- 514 Kim HG, Patel VC, Lee CM (2000) Numerical simulation of wind flow
515 over hilly terrain. *Journal of wind engineering and industrial aerodynamics*
516 87(1):45–60
- 517 Lancaster LNSM J (1984) Climate of the central namib desert. *Madoqua*
518 1984(1):5–61
- 519 Lancaster N (1985) Winds and sand movements in the namib sand sea. *Earth
520 Surface Processes and Landforms* 10(6):607–619
- 521 Lewis HW, Mobbs SD, Lehning M (2008) Observations of cross-ridge flows
522 across steep terrain. *Quarterly Journal of the Royal Meteorological Society:
523 A journal of the atmospheric sciences, applied meteorology and physical
524 oceanography* 134(633):801–816
- 525 Liu ZYC, Zimbelman JR (2015) Recent near-surface wind directions inferred
526 from mapping sand ripples on martian dunes. *Icarus* 261:169–181
- 527 Livingstone I, Warren A (1996) Aeolian geomorphology: an introduction. Ad-
528 dison Wesley Longman Ltd
- 529 Livingstone I, Bristow C, Bryant RG, Bullard J, White K, Wiggs GFS, Baas
530 ACW, Bateman MD, Thomas DSG (2010) The namib sand sea digital
531 database of aeolian dunes and key forcing variables. *Aeolian Research* 2(2-
532 3):93–104
- 533 Lorenz R, Claudin P, Andreotti B, Radebaugh J, Tokano T (2010) A 3 km
534 atmospheric boundary layer on titan indicated by dune spacing and huygens
535 data. *Icarus* 205(2):719–721
- 536 Lü P, Narteau C, Dong Z, Rozier O, Du Pont SC (2017) Unravelling raked
537 linear dunes to explain the coexistence of bedforms in complex dunefields.
538 *Nature communications* 8(1):1–9
- 539 Lü P, Narteau C, Dong Z, Claudin P, Rodriguez S, An Z, Fernandez-Cascales
540 L, Gadale C, Courrech du Pont S (2021) Direct validation of dune instability
541 theory. *Proceedings of the National Academy of Sciences* 118(17)
- 542 McKee ED (1979) A study of global sand seas, vol 1052. US Government
543 Printing Office
- 544 Muñoz-Sabater J, Dutra E, Agustí-Panareda A, Albergel C, Arduini G, Bal-
545 samo G, Boussetta S, Choulga M, Harrigan S, Hersbach H, et al. (2021)
546 Era5-land: A state-of-the-art global reanalysis dataset for land applications.
547 *Earth System Science Data Discussions* pp 1–50

- 548 Pähzt T, Durán O (2020) Unification of aeolian and fluvial sediment transport
549 rate from granular physics. *Physical review letters* 124(16):168,001
- 550 Pearce KI, Walker IJ (2005) Frequency and magnitude biases in the 'Fryberger'
551 model, with implications for characterizing geomorphically effective winds.
552 *Geomorphology* 68(1-2):39–55, DOI 10.1016/j.geomorph.2004.09.030
- 553 Pelletier JD, Field JP (2016) Predicting the roughness length of turbulent flows
554 over landscapes with multi-scale microtopography. *Earth Surface Dynamics*
555 4(2):391–405, DOI 10.5194/esurf-4-391-2016
- 556 Rasmussen KR, Iversen JD, Rautaheimo P (1996) Saltation and wind flow
557 interaction in a variable slope wind tunnel. *Geomorphology* 17:19–28
- 558 Rubin DM, Hunter RE (1987) Bedform alignment in di-
559 rectinally varying flows. *Science* 237:276–278, DOI
560 <https://doi.org/10.1126/science.237.4812.276>
- 561 Runyon K, Bridges N, Ayoub F, Newman C, Quade J (2017) An integrated
562 model for dune morphology and sand fluxes on mars. *Earth and Planetary
563 Science Letters* 457:204–212
- 564 Seidel DJ, Zhang Y, Beljaars A, Golaz JC, Jacobson AR, Medeiros B (2012)
565 Climatology of the planetary boundary layer over the continental united
566 states and europe. *Journal of Geophysical Research: Atmospheres* 117(D17)
- 567 Shao Y (2008) Physics and modelling of wind erosion, vol 37. Springer Science
568 & Business Media
- 569 Shen Y, Zhang C, Huang X, Wang X, Cen S (2019) The effect of wind speed
570 averaging time on sand transport estimates. *Catena* 175:286–293
- 571 Sheridan PF, Vosper SB (2006) A flow regime diagram for forecasting lee
572 waves, rotors and downslope winds. *Meteorological Applications* 13(2):179–
573 195
- 574 Sherman DJ, Farrell EJ (2008) Aerodynamic roughness lengths over movable
575 beds: Comparison of wind tunnel and field data. *Journal of Geophysical
576 Research: Earth Surface* 113(2):1–10, DOI 10.1029/2007JF000784
- 577 Sherman DJ, Li B (2012) Predicting aeolian sand transport rates: A reevalu-
578 ation of models. *Aeolian Research* 3(4):371–378
- 579 Smith AB, Jackson DWT, Cooper JAG (2017) Three-dimensional airflow and
580 sediment transport patterns over barchan dunes. *Geomorphology* 278:28–42
- 581 Song Q, Gao X, Lei J, Li S (2019) Spatial distribution of sand dunes and their
582 relationship with fluvial systems on the southern margin of the taklimakan
583 desert, china. *Geomatics, Natural Hazards and Risk* 10(1):2408–2428
- 584 Spalding DB (1961) A single formula for the "law of the wall"
- 585 Stull R (2006) 9 - the atmospheric boundary layer. In: Wallace JM, Hobbs
586 PV (eds) *Atmospheric Science* (Second Edition), second edition edn, Aca-
587 demic Press, San Diego, pp 375–417, DOI <https://doi.org/10.1016/B978-0-12-732951-2.50014-4>
- 588 Stull RB (1988) An introduction to boundary layer meteorology, vol 13.
589 Springer Science & Business Media
- 590 Sullivan PP, McWilliams JC (2010) Dynamics of winds and currents coupled
591 to surface waves. *Annual Review of Fluid Mechanics* 42:19–42

- 593 Sykes RI (1980) An asymptotic theory of incompressible turbulent boundary-
594 layer flow over a small hump. *Journal of Fluid Mechanics* 101(3):647–670
595 Ungar JE, Haff PK (1987) Steady state saltation in air. *Sedimentology* 34:289–
596 299
597 Unsworth C, Parsons D, Hardy R, Reesink A, Best J, Ashworth P, Keevil G
598 (2018) The impact of nonequilibrium flow on the structure of turbulence
599 over river dunes. *Water Resources Research* 54(9):6566–6584
600 Uppala SM, Källberg P, Simmons AJ, Andrae U, Bechtold VDC, Fiorino M,
601 Gibson J, Haseler J, Hernandez A, Kelly G, et al. (2005) The era-40 re-
602 analysis. *Quarterly Journal of the Royal Meteorological Society: A journal*
603 of the atmospheric sciences, applied meteorology and physical oceanography
604 131(612):2961–3012
605 Virtanen P, Gommers R, Oliphant TE, Haberland M, Reddy T, Cournapeau
606 D, Burovski E, Peterson P, Weckesser W, Bright J, et al. (2020) Scipy 1.0:
607 fundamental algorithms for scientific computing in python. *Nature methods*
608 17(3):261–272
609 Vosper SB (2004) Inversion effects on mountain lee waves. *Quarterly Journal*
610 of the Royal Meteorological Society: A journal of the atmospheric sciences,
611 applied meteorology and physical oceanography 130(600):1723–1748
612 Walker IJ, Shugar DH (2013) Secondary flow deflection in the lee of transverse
613 dunes with implications for dune morphodynamics and migration. *Earth*
614 surface processes and landforms 38(14):1642–1654
615 Walker IJ, Hesp PA, Davidson-Arnott RG, Bauer BO, Namikas SL,
616 Ollerhead J (2009) Responses of three-dimensional flow to variations
617 in the angle of incident wind and profile form of dunes: Greenwich
618 dunes, prince edward island, canada. *Geomorphology* 105:127–138, DOI
619 10.1016/j.geomorph.2007.12.019
620 Zhang C, Li Q, Zhou N, Zhang J, Kang L, Shen Y, Jia W (2016) Field obser-
621 vations of wind profiles and sand fluxes above the windward slope of a sand
622 dune before and after the establishment of semi-buried straw checkerboard
623 barriers. *Aeolian Research* 20:59–70, DOI 10.1016/j.aeolia.2015.11.003
624 Zilker DP, Hanratty TJ (1979) Influence of the amplitude of a solid wavy wall
625 on a turbulent flow. part 2. separated flows. *Journal of Fluid Mechanics*
626 90(2):257–271
627 Zilker DP, Cook GW, Hanratty TJ (1977) Influence of the amplitude of a solid
628 wavy wall on a turbulent flow. part 1. non-separated flows. *Journal of Fluid*
629 *Mechanics* 82(1):29–51

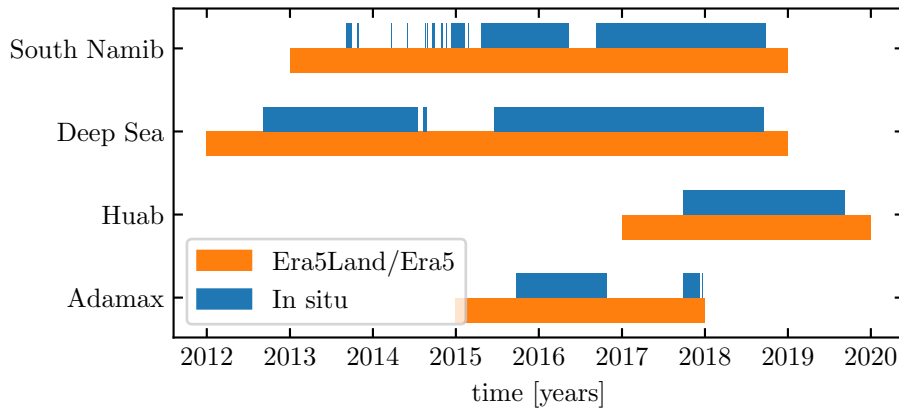


Fig. S1 Gant chart representing the valid time steps for the two data sets, for all stations.

630 **Supplementary Material for *Boundary-Layer Meteorology* Sample
631 Paper: Instructions for Authors**

632 **First Author* · Second Author · Third Author**

633
634 *Affiliation and email address for the corresponding author only (note that
635 the corresponding author does not need to be the first author).

636 **1. Shear velocity and calibration of the hydrodynamical roughness**

637 As the regionally predicted and locally measured velocities are available at
638 different heights, we can not compare them directly. We then convert all ve-
639 locities into shear velocities u_* , characteristic of the turbulent velocity profile
640 (Spalding 1961; Stull 1988):

$$\frac{u(z)}{u_*} = \frac{1}{\kappa} \ln \left(\frac{z}{z_0} \right), \quad (16)$$

641 where z is the vertical coordinate, $\kappa \approx 0.4$ the von Kármán constant and
642 z_0 the hydrodynamic roughness. Several field measurements of hydrodynamic
643 roughnesses are available. In the absence of sediment transport, it scales with
644 the geometric roughness of the topography (Pelletier and Field 2016). When
645 transport occurs, it then scales with the thickness of the transport layer (\sim
646 1 mm), depending on the wind velocity and grain properties (Sherman and
647 Farrell 2008; Zhang et al. 2016; Field and Pelletier 2018).

648 The different environments of our stations (vegetated, arid, sandy) makes
649 it difficult to develop a precise model for the computation of the hydrodynamic
650 roughness. Furthermore, we do not have precise enough topographical mea-
651 surements that would allow to compute the geometric roughness. We choose

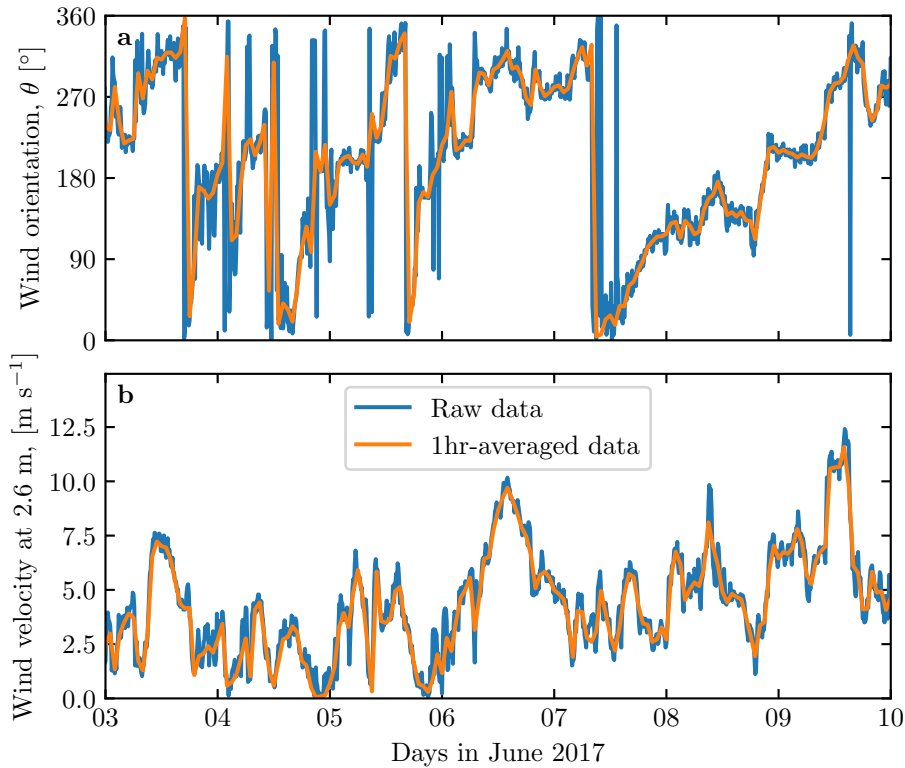


Fig. S2 Comparison between raw local wind measurements, and centered averaged data over one hour for the South Namib station. **a:** wind direction. **b:** wind velocity at the measurement height, 2.6 m.

652 to leave aside this complexity, and use a different approach. The selected hydrodynamic roughness is then the one that leads to the best possible matching
 653 between the regionally predicted and locally measured winds.
 654

655 For each station, the hydrodynamic roughness is calibrated by finding the
 656 one that minimizes the relative difference δ between the wind vectors of both
 657 datasets:

$$\delta = \frac{\sqrt{\langle \|\mathbf{u}_{*,\text{era}} - \mathbf{u}_{*,\text{station}}\|^2 \rangle_t}}{\sqrt{\langle \|\mathbf{u}_{*,\text{era}}\| \rangle_t \langle \|\mathbf{u}_{*,\text{station}}\| \rangle_t}} \quad (17)$$

658 This δ -parameter is computed for hydrodynamic roughness values ranging
 659 from 10^{-5} m to 10^{-2} m for the different stations. Note that for the Deep Sea
 660 and South Namib stations, where the giant dunes feedback presumably affect
 661 the wind, we take into account the non-deflected winds only in the calculation
 662 of δ (with a 15° tolerance).

663 A shown by figure S3, the minimum of δ in the space (z_0^{Era5Land} , z_0^{local})
 664 forms a line. We thus take the roughness of the Era5Land dataset as the typical
 665 value when sediment transport occurs, 10^{-3} m, corresponding to the thickness
 666 of the transport layer (Durán et al. 2011). It leads for the Adamax, Deep Sea,

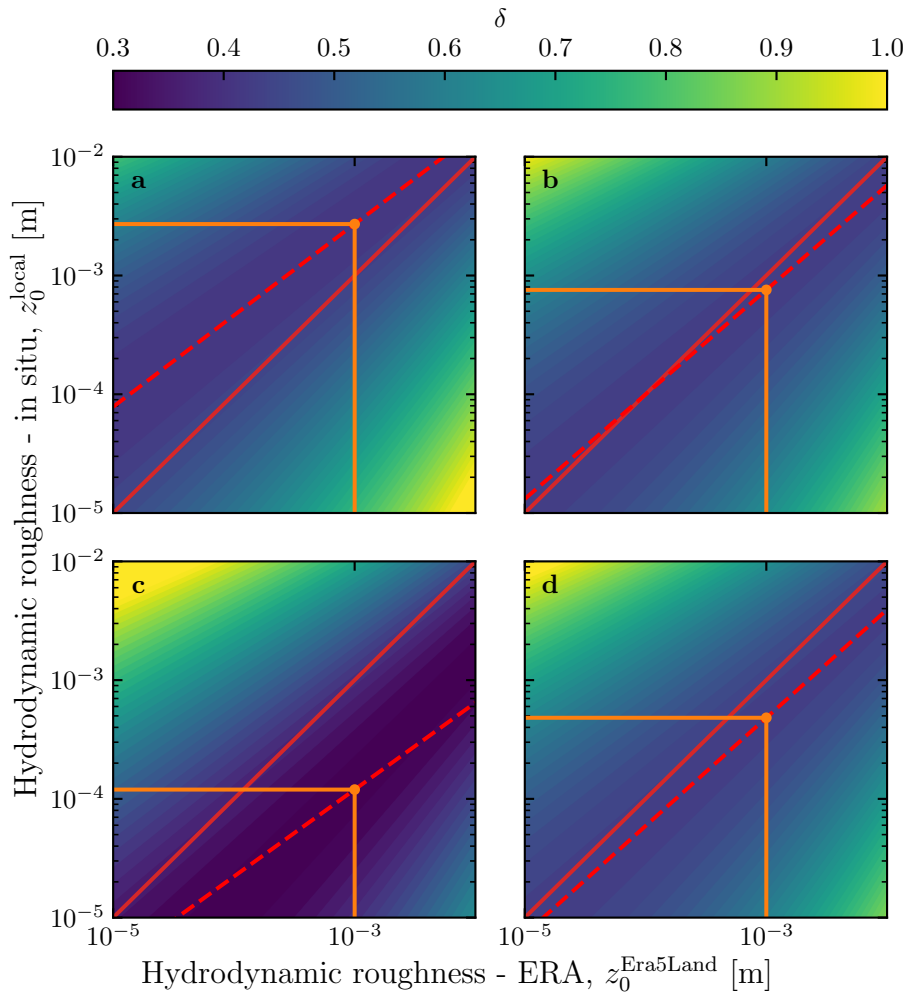


Fig. S3 Calibration of the hydrodynamic roughnesses. The metric δ defined in (17) is represented in colorscale as a function of the hydrodynamic roughnesses chosen for the Era5-Land and local winds, for the (a) Adamax, (b) Deep Sea, (c) Huab and (d) South Namib stations. The red dashed and plain lines shows the minima of δ and the identity line, respectively. The orange lines and dots highlight the chosen hydrodynamic roughnesses for the local winds, by imposing $z_0^{\text{Era5Land}} = 1 \text{ mm}$. It leads for each station to 2.7 mm, 0.76 mm, 0.12 mm and 0.48 mm, respectively.

667 Huab and South Namib stations values of 2.7 mm, 0.76 mm, 0.12 mm and
668 0.48 mm, respectively.

669 The choice of the hydrodynamic roughness values impacts the calculated
670 shear velocities only, but not the wind directions. As such, most of our conclu-
671 sions are independent of such a choice. However, it may affect the magnitude
672 of the wind velocity attenuation/amplification in flow confinement situations.

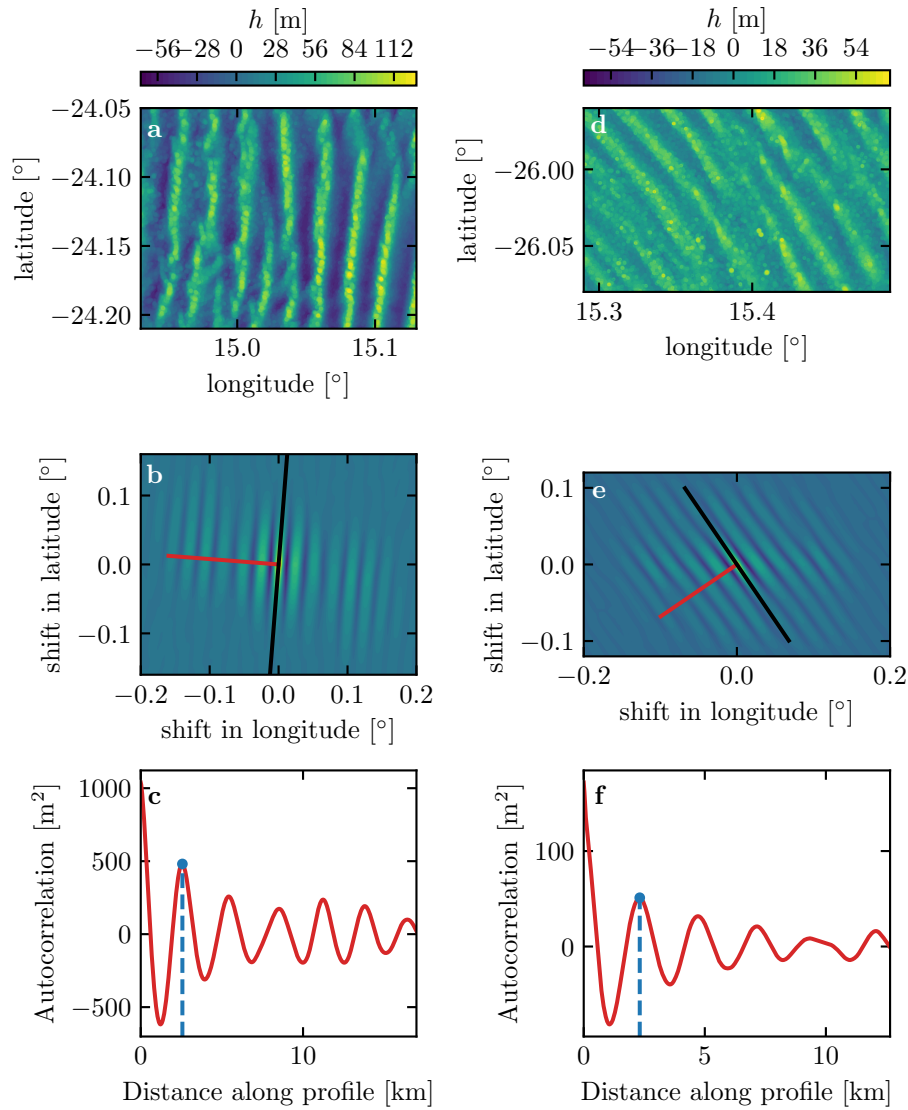


Fig. S4 Analysis of the DEMs of the Deep Sea (left column – **a**, **b**, **c**) and South Namib (right column – **d**, **e**, **f**) stations. **a–d**: Detrended topography (a second order polynomial is first fitted and then removed). **b–e**: autocorrelation matrix shown in colorscale. The black line shows the detected orientation, and the red line the profile along which the wavelength is calculated, shown in **c–f**. The blue lines and dots show the first peak of the autocorrelation profile, whose abscissa gives the characteristic wavelength of the dune pattern.

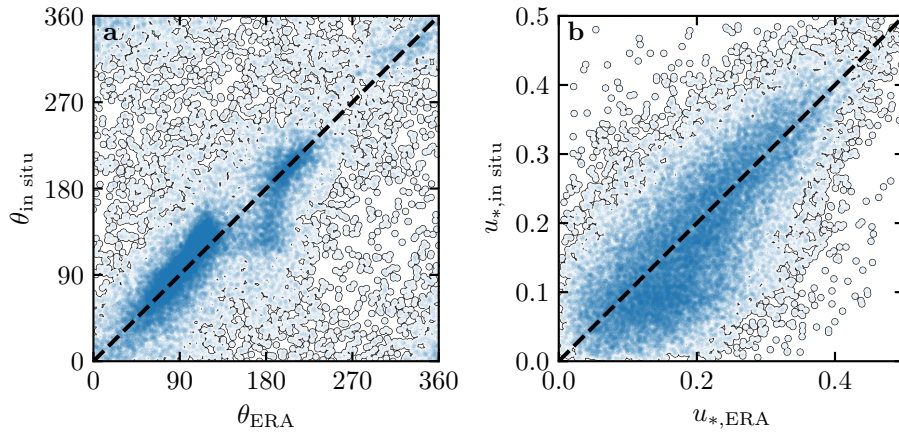


Fig. S5 Statistical agreement of the wind orientation (a) and velocity (b) between the Era5Land dataset and the local measurements for the Huab and Adamax stations. Note how the points are clustered around identity lines (dashed and black).

673 2. Extraction of the ABL properties

674 The estimation of the non-dimensional numbers requires the computation of
 675 meteorological quantities representative of the current atmospheric boundary
 676 layer. In arid areas, the vertical structure of the atmosphere can be approxi-
 677 mated by well mixed convective boundary layer of height H , topped by the
 678 stratified free atmosphere (Stull 1988; Shao 2008). In this type of structure,
 679 the virtual potential temperature is constant inside the boundary layer, and
 680 then increases linearly in the stratified free atmosphere (Fig. S9a):

$$T_{\text{vp}}(z) = \begin{cases} T_0 & \text{for } z < H, \\ T_0 \left(1 + \frac{\Delta T_{\text{vp}}}{T_0} + \frac{N^2}{g}(z - H) \right) & \text{for } z > H, \end{cases} \quad (18)$$

681 where, T_0 is the surface virtual potential temperature, ΔT_{vp} the discontinuity
 682 at the capping layer and N the Brunt-Väisälä frequency, characteristic of the
 683 stratification.

684 The Era5 dataset provides a direct estimate of the ABL depth H from a
 685 bulk Richardson number calculation, as well as vertical profiles of the geo-
 686 potential ϕ , temperature T and specific humidity e_w at given pressure levels P .
 687 From these quantities, the virtual potential temperature can be calculated as:

$$T_{\text{vp}} = T (1 + [R_M - 1] e_w) \left(\frac{P_0}{P} \right)^{P_c(1-0.24e_w)}, \quad (19)$$

688 where $P_0 = 10^5$ Pa is the standard pressure, $P_c = 0.2854$ the Poisson coefficient
 689 for dry air and $R_M = 1.61$ is the ratio between the molecular masses of dry

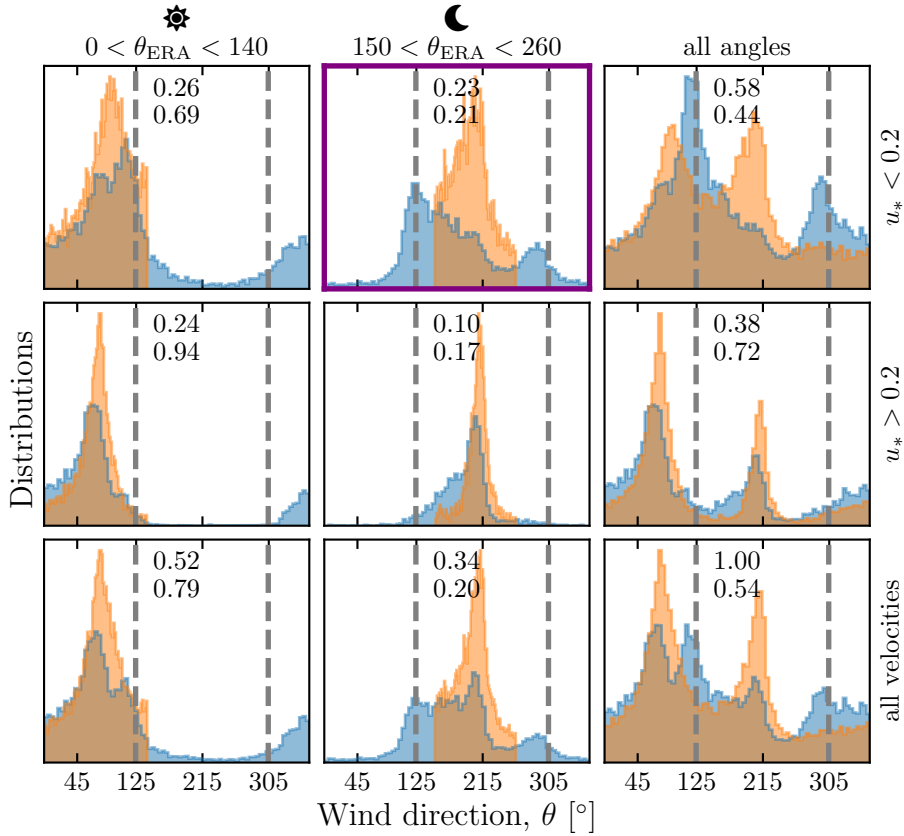


Fig. S6 Distributions of wind direction at the South Namib Station for the Era5Land climate reanalysis (orange) and the local measurements (blue). In each subplot, both distributions are plotted from the same time steps, selected with constraints on the wind direction (columns) and/or wind velocity (rows) in the Era5Land dataset. The gray vertical dashed lines indicate the dune orientation. The numbers at the top center give the percentage of time steps selected in each sub-range, as well as the percentage of them corresponding to the day (between 1000 UTC and 2200 UTC). The purple frame highlights the regime (small wind velocities, nocturnal summer wind) during which the wind data from both datasets differs. A similar figure can be obtained for the South Namib station (see Fig. 3).

690 air and water. The vertical coordinates are calculated as:

$$z = \frac{\phi R_t}{g R_t - \phi}, \quad (20)$$

691 where $R_t = 6356766$ m is the average Earth radius, and $g = 9.81$ m s⁻² the
692 gravitational acceleration.

693 Example of obtained vertical profiles of the virtual potential temperature
694 are shown in Fig. S9a. On each of them, an average is computed below the ABL
695 depth directly given by the Era5 dataset, and a linear function is fitted above.
696 Note that under the Boussinesq approximation, the temperature variations are

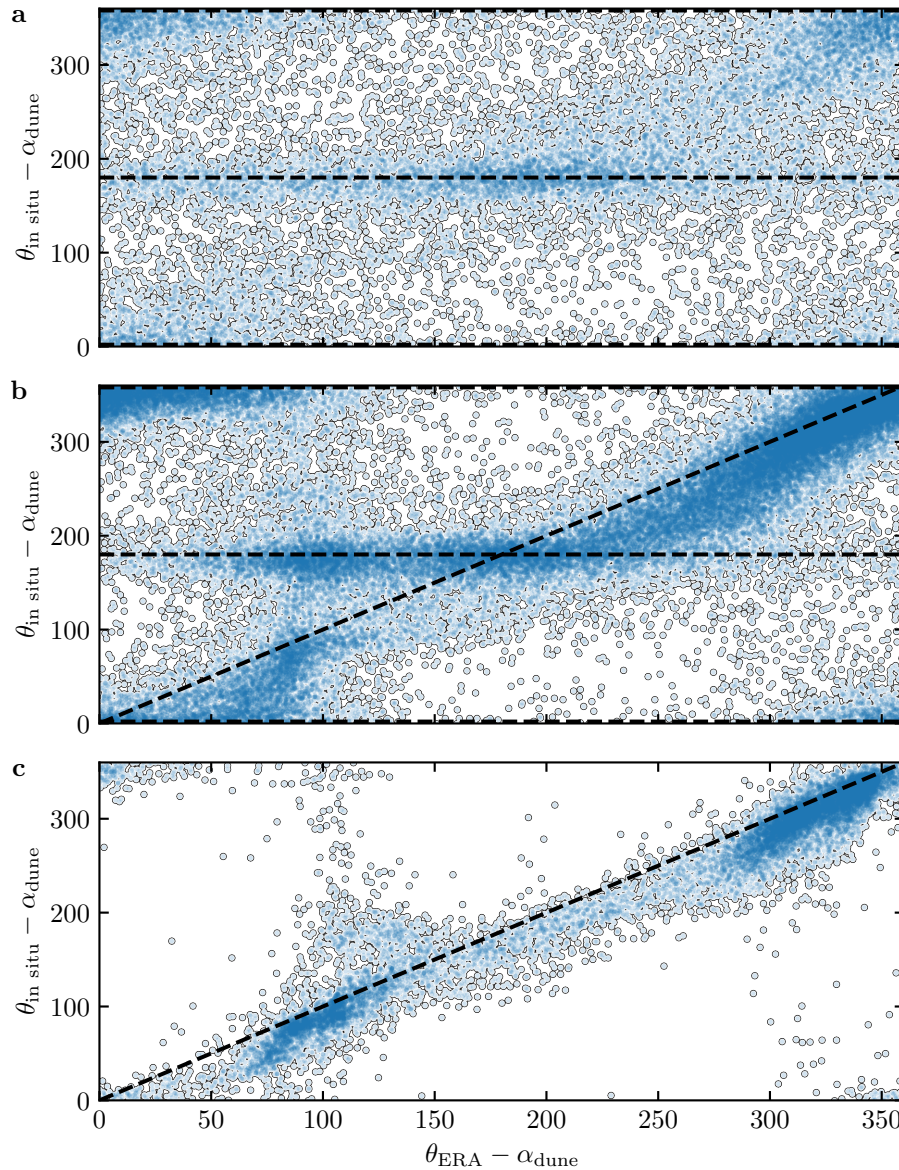


Fig. S7 Statistical comparison of the wind orientation between the Era5Land dataset and the local measurements for the South Namib and Deep Sea stations, for different velocity ranges. **a:** $u_{*,\text{ERA}} < 0.1 \text{ m s}^{-1}$. **b:** $0.1 < u_{*,\text{ERA}} \leq 0.25 \text{ m s}^{-1}$. **c:** $u_{*,\text{ERA}} \geq 0.25 \text{ m s}^{-1}$. Note that the measured dune orientations are subtracted to the wind orientation, which allows to plot both stations on the same graph. Black dashed lines indicate locally measured orientations aligned with the dune crests (here 0° , 180° and 360° – **a, b**), as well as the identity lines (**b, c**).

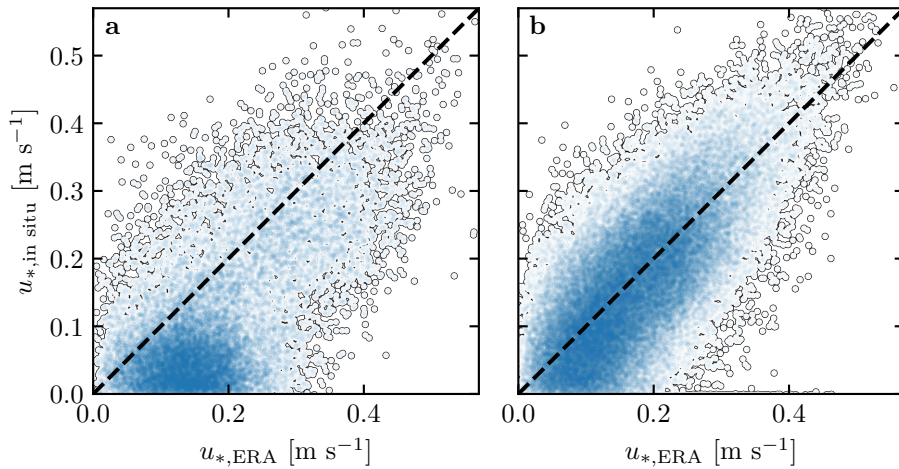


Fig. S8 Statistical comparison of the wind velocity between the Era5Land dataset and the local measurements for the South Namib and Deep Sea stations. **a:** Nocturnal summer easterly wind. **b:** Diurnal southerly wind. Black dashed lines are identity lines. The angle ranges used to select diurnal and nocturnal summer winds are those taken in Fig. 3 and Fig. S6.

assumed to induce most of those of the density, leading to $\Delta\rho/\rho_0 \simeq \Delta T_{\text{vp}}/T_0$ (see supplementary material of (Andreotti et al. 2009)). Note that we removed some profiles that displayed a vertical structure that could not be approximated by the simple model used here, leading for example to negative values of ΔT_{vp} (see Fig. S9b). While these profiles dominantly occurs in winter, when the two winds blows, they are evenly spread across the hours of the day, and represent 12 % of our data only (see Fig. S9c–d). For these reasons, we are confident this does not affect pour conclusions.

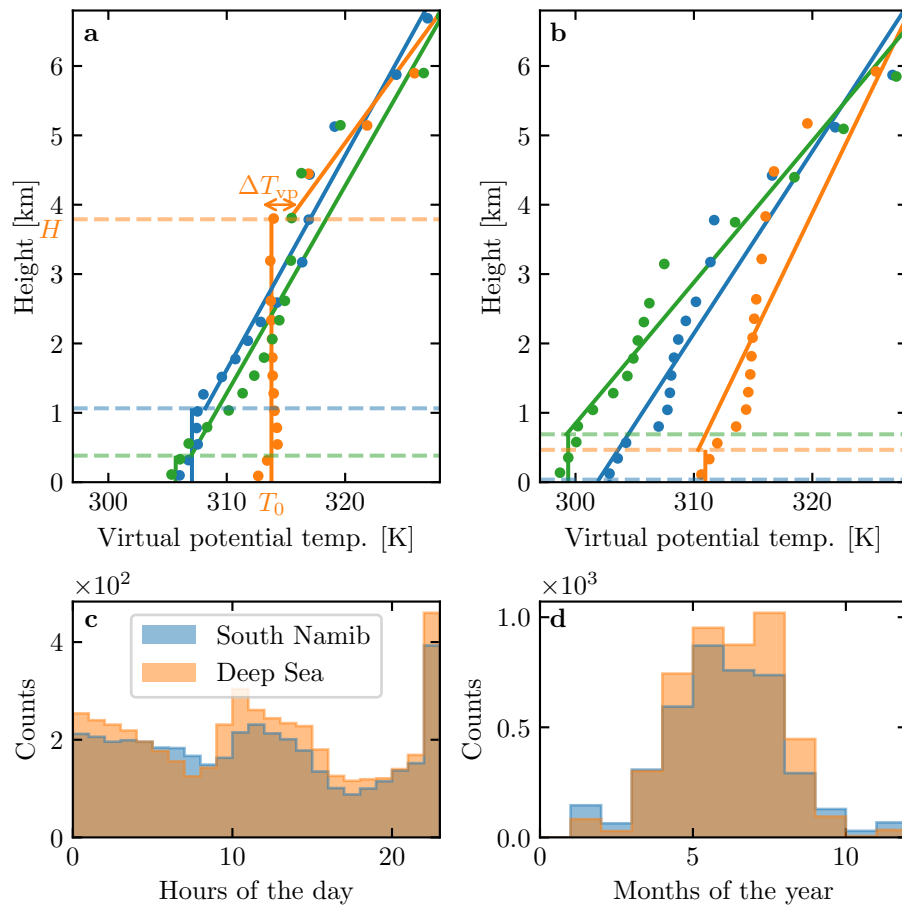


Fig. S9 **a:** Vertical profiles of the virtual potential temperature at 3 different time steps (blue - 29/11/2012 - 1100 UTC, orange - 21/03/2017 - 1200 UTC, green - 21/03/2017 - 2000 UTC) at the South Namib station. Dots: data from the ERA5 reanalysis. Transparent dashed lines: boundary layer height given by the ERA5 reanalysis, calculated from the bulk Richardson number (Seidel et al. 2012). Plain lines: vertical (ABL) and linear (FA) fits to estimate the quantities in Fig. S10. **b:** Examples of ill-processed vertical profiles at 3 different time steps (blue - 2/12/2013 - 2300 UTC, orange - 20/03/2017 - 0000 UTC, green - 14/07/2017 - 1400 UTC) at the South Namib station. **c:** Hourly distribution of ill-processed vertical profiles. **d:** Monthly distribution of ill-processed vertical profiles.

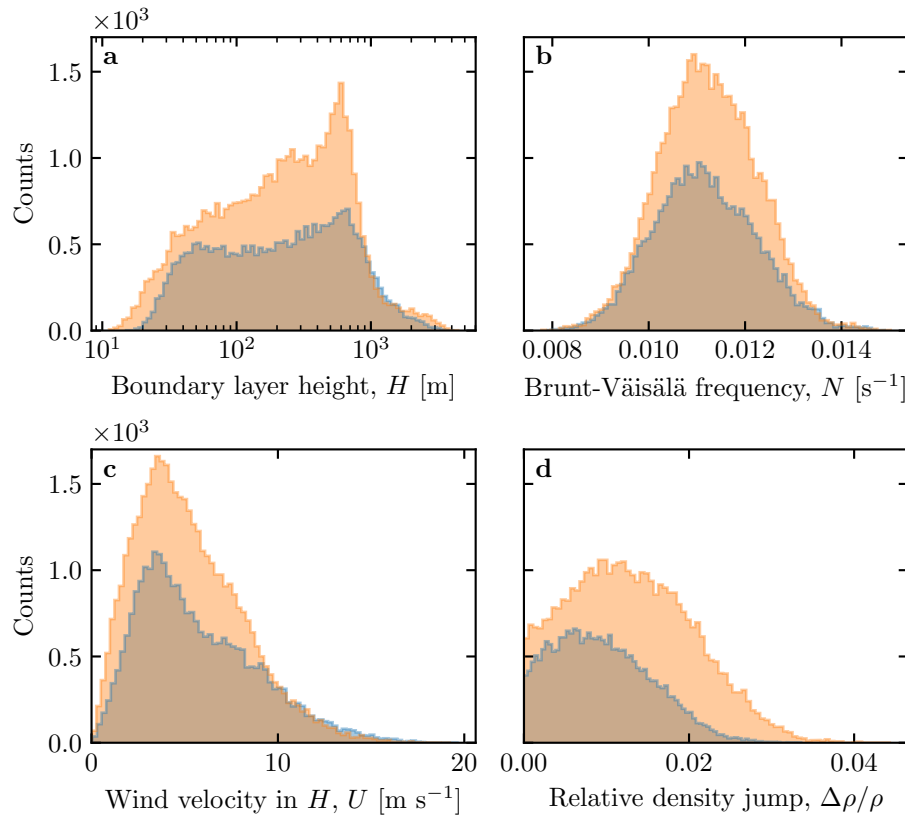


Fig. S10 Distributions of the meteorological parameters resulting from the processing of the Era5-Land data for the South Namib (blue) and the Deep Sea (orange) stations.

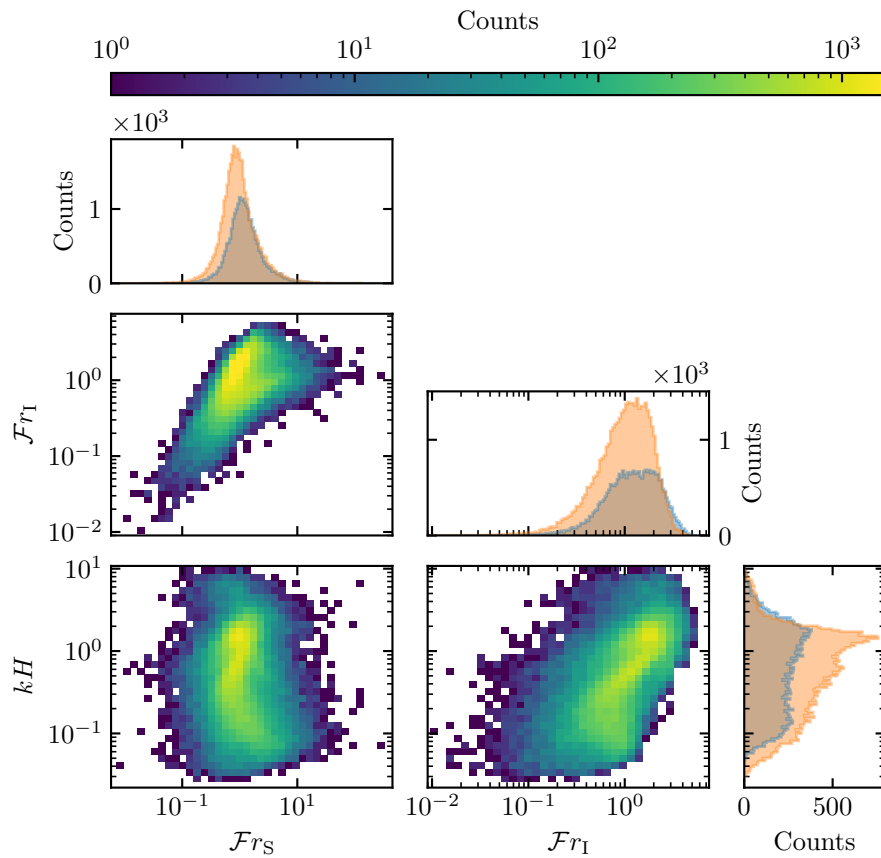


Fig. S11 Non-dimensional parameters distributions. For the marginal distributions, the orange correspond to the South Namib station, and the blue to the Deep Sea station.

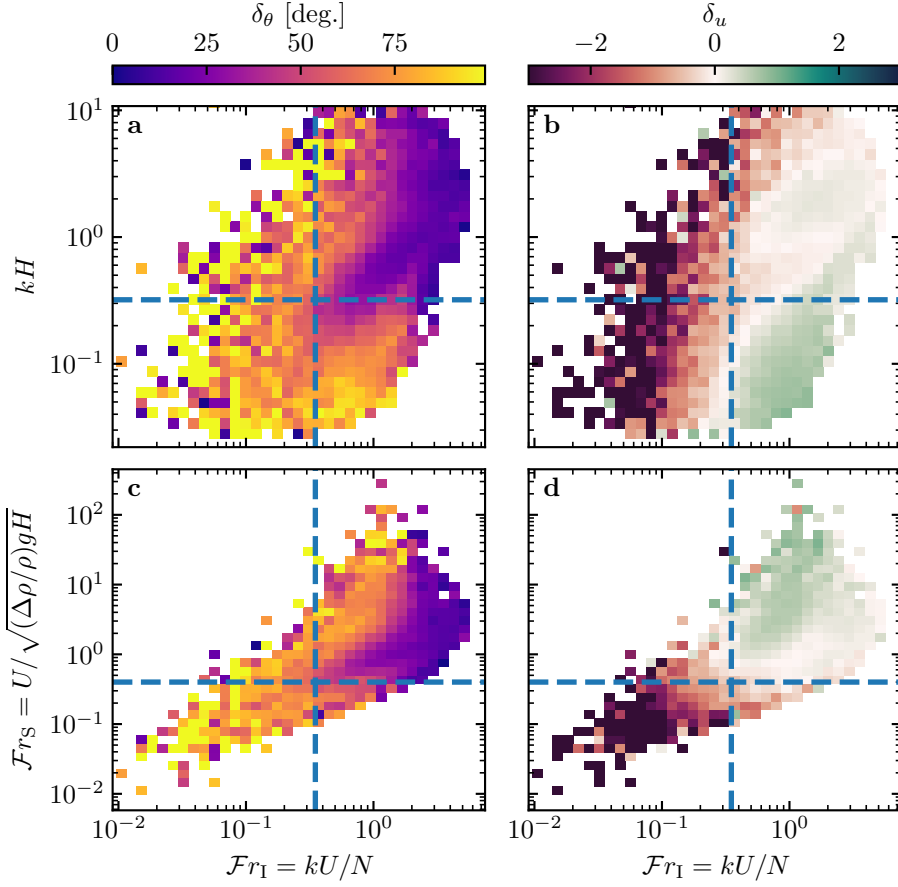


Fig. S12 Regime diagrams of the wind deviation δ_θ and relative attenuation/amplification δ_u in the spaces (\mathcal{F}_I, kH) and $(\mathcal{F}_I, \mathcal{F})$, containing the data from both the Deep Sea and South Namib stations. Blue dashed lines empirically delimit the different regimes. The point density in each bin of the diagrams is shown in Fig. S11. The regime diagrams in the space (\mathcal{F}, kH) are shown in Fig. 5 of the main article.

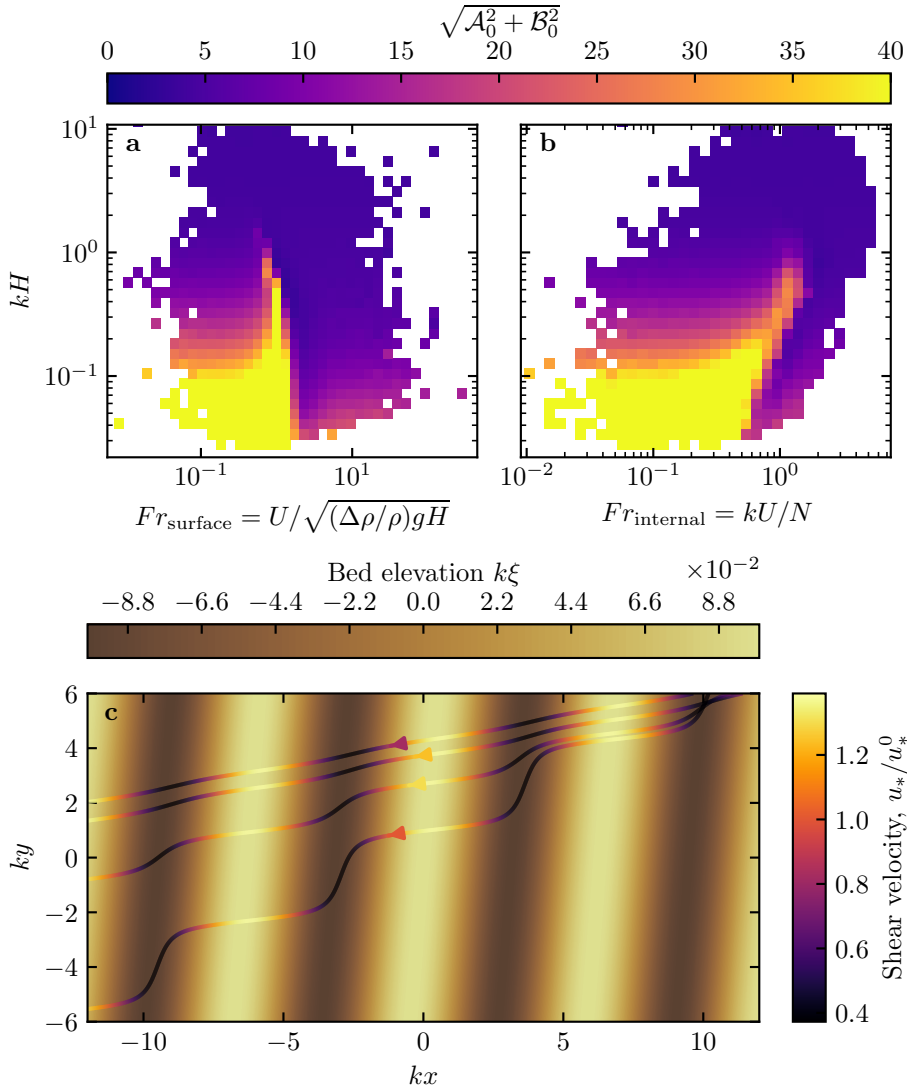


Fig. S13 Physical interpretation of the flow disturbance. (a) and (b) Magnitude of the disturbance induced by a sinusoidal topography calculated from the time series of the non-dimensional numbers presented in Figures 4 and 5 using the linear model of Andreotti et al. (2009). (c) Shear velocity streamlines represented in the case of the Deep Sea station, for increasing values of $\sqrt{\mathcal{A}_0^2 + \mathcal{B}_0^2}$. From the upper to the lower streamline, values of $(kH, Fr_{\text{surface}}, Fr_{\text{internal}}, \mathcal{A}_0, \mathcal{B}_0, \sqrt{\mathcal{A}_0^2 + \mathcal{B}_0^2})$ are $(1.9, 0.6, 1.5, 3.4, 1.0, 3.5)$, $(1.5, 0.3, 0.4, 4.8, 1.4, 5.0)$, $(0.1, 3.5, 1.0, 8.6, 0.1, 8.6)$, $(0.5, 0.05, 0.04, 9.6, 2.5, 9.9)$.